J. Fluid Mech. (1996), vol. 320, pp. 71–115

Measurements of spatiotemporal dynamics in a forced plane mixing layer

By SATISH NARAYANAN AND FAZLE HUSSAIN
Department of Mechanical Engineering, University of Houston, Houston, TX 77204–4792, USA

(Received 19 September 1994 and in revised form 23 February 1996)

We present an approach combining temporal dynamical systems methods with newly proposed spatial coupling measures – namely, coherence and cross-bicoherence – to identify and quantitatively describe low-dimensional dynamics in transitional *open* flows. The approach is used to describe a forced mixing layer as a low-dimensional temporal dynamical system and interpret its transitional vortex dynamics.

Experiments were performed in an initially laminar plane mixing layer inside an anechoic chamber using forcing of the fundamental instability only; the forcing frequency and amplitude are used as control parameters. Dynamical invariants calculated show that vortex roll-up and the feedback-driven first two pairing dynamics are well-described by one periodic and at least two low-dimensional chaotic attractors; a phase diagram delineating such dynamical states in the control parameter space is presented. The large spatial extents of these feedback-sustained states (verified using coherence and cross-bicoherence), spanning many instability wavelengths downstream, indicate spatial coupling; feedback has also been experimentally verified. At a fixed forcing frequency, as the forcing amplitude is decreased, the spatially coupled, periodic second pairing dynamics becomes chaotic and spatiotemporal (inferred from decay of coherence and cross-bicoherence); the dynamics in the domain that includes the first pairing, however, remains temporal. This loss of spatial coupling is accompanied by a sudden increase in the attractor dimension, and suggests spatiotemporal chaos. The combination of dynamical systems theory and spatial measures seems to be a promising approach to probe spatiotemporal dynamics in other open flows as well.

1. Introduction

The dynamical systems (DS) approach has been applied successfully to identify low-dimensional temporal dynamics in closed flows (e.g. Dubois 1982; Brandstäter *et al.* 1983). The problem with a DS description of technologically significant open flows (such as jets, mixing layers and boundary layers) is that their convectively unstable nature makes them sensitive to external noise. (Noise includes disturbances originating external to the domain of interest, e.g. wind tunnel and laboratory room acoustics, blower-originated pulsations.) Consequently, spatially amplified random noise may not be distinguishable from intrinsic low-dimensional chaos (Huerre 1987), and standard DS tools to detect temporal chaos may fail (Deissler & Kaneko 1987). On the other hand, flows with global instabilities are readily amenable to the temporal DS approach. In the following, we first review the concepts of 'local' and 'global' instabilities in spatially developing flows. We then describe the limitations in using these ideas to probe open flows and motivate the need for a new approach, and then explain our approach.

Huerre & Monkewitz (1990, hereinafter referred to as HM) studied two types of local instability: absolute and convective. Disturbances in an absolutely unstable flow dominate the dynamics at their origin and eventually everywhere in the domain, while in convectively unstable flows, disturbances are swept away from the origin. HM then studied the instability of a weakly non-parallel base flow extending over a 'large' region (over a few instability wavelengths), namely, a 'global instability'. In the absence of long-range pressure feedback (e.g. edge-tone flows), they concluded that the existence of an unstable global mode 'necessarily implied a finite region of absolute instability' (see also Monkewitz, Huerre & Chomaz 1993). In contrast, flows that are convectively unstable everywhere were said to be globally stable wherein no self-sustained states arise, e.g. channel flows. Global instability was claimed to result in self-excited oscillations (at a global frequency) of a large flow region. An equivalent viewpoint regards the global mode as a time-periodic solution of the linearized disturbance equations for a non-parallel base flow. In the experimental study of a near wake, Mathis, Provansal & Boyer (1984) used the Stuart–Landau equation to describe the oscillation amplitude. Schumm, Berger & Monkewitz (1994) also conducted similar studies, but admit that the frequency and the growth rate of the global mode obtained from experiments could not be verified using the theoretical analyses of HM and Monkewitz *et al.* (1993) owing to violation of the weakly non-parallel flow assumption in the laboratory flow. Global modes were also inferred experimentally in non-uniform density jets (Monkewitz *et al.* 1990) where the occurrence of an absolute instability was well known. However, it was only speculated that convectively unstable, uniform-density jets sustained a global mode (upon small forcing) related to a 'slightly damped jet-column mode' (HM).

Implicit in global instability analyses is the dominance of a single mode in the flow domain. The occurrence of various instabilities in some open shear flows causes different frequencies to dominate at different spatial locations, e.g. fundamental (Kelvin–Helmholtz) and successive subharmonic (nonlinear) instabilities in a mixing layer or a jet cause vortex formation and their interactions, respectively, at different locations (with different timescales). The presence of multiple frequencies (none of which dominates everywhere) suggests that such open flows are incapable of sustaining global modes. Furthermore, since open flows such as jets and boundary layers are highly non-parallel, global instability analyses for these flows are not feasible. In fact, HM claim that a breakdown of the weakly non-parallel assumption 'would preclude any possible connection between local and global instability properties'. Consequently, the concept of global instability is applicable only to a narrow class of flows which are weakly (spatially) inhomogeneous and typically absolutely unstable. Yet, the most interesting open flows (from the technological point of view) are spatially inhomogeneous (highly non-parallel), in addition to being locally convectively unstable. Establishing definite relations between local dynamics and dynamics observed over large spatial extents in open flows would allow exploration of low-dimensional dynamics via the nonlinear DS approach and may hence permit control of these seemingly complex spatiotemporal flows. In this regard, although the study of global instabilities has improved our understanding of some spatially developing flows (e.g. wakes), this approach is inadequate for describing technologically significant open flows such as jets, mixing layers and boundary layers.

Temporal DS techniques can be used to detect low-dimensional chaos in open flows with global modes, e.g. in the absolutely unstable near wake of a cylinder (Van Atta & Gharib 1987). However, since disturbances in a locally convectively unstable flow advect and leave their origin (point of receptivity) susceptible to new disturbances, such a flow is extremely sensitive to external noise. Dynamical invariants, extracted from single-point measurements, in such flows can be used at most to predict the local dynamical state (i.e. in a region much smaller than the domain of interest). To fully describe a convectively unstable flow, it is necessary to sample data simultaneously at several locations spanning the entire flow domain. Despite this limitation, Bonetti & Boon (1989) (in a Poiseuille-profile jet) and Williams-Stuber & Gharib (1990) (in an airfoil wake) used DS analyses of single-point measurements to describe the open flows in terms of low-dimensional temporal attractors. No attempt was made by those authors to study the spatial extent of the identified dynamical states; such an experimental description is not useful if the low-dimensional states capture flow organization which is only local. To resolve ambiguities in applying DS tools to open flows, it is necessary to start with a prototypical flow which is otherwise well-documented through conventional measures and is of substantial fundamental and technological interest. We have thus chosen to study a plane mixing layer (ML) owing to its simple features (e.g. single lengthscale θ_e, the exit momentum thickness) and extensive studies as a reference flow (see, for example, Oster & Wygnanski 1982; Ho & Huerre 1984). We now present our approach to analyse low-dimensional dynamics in open flows.

Our approach is motivated by the fact that convectively unstable open flows can also display intrinsic dynamics, namely, via feedback. Strong feedback may come from flow interaction with solid boundaries (e.g. the jet edge-tone phenomenon (Brown 1937); the shear-layer tone phenomenon (Hussain & Zaman 1978)), dynamical events within the flow itself such as vortex roll-up and pairing (e.g. experiments of Dimotakis & Brown (1976) and simulations of Grinstein, Oran & Boris (1991)) or could be electronically imposed (Reisenthel 1988). Broze & Hussain (1994, hereinafter referred to as BH) justified a temporal DS description of a forced axisymmetric jet (an open flow) with a conceptual model incorporating the feedback due to vortex pairings.

We propose that an open flow with spatial coupling behaves as a temporal dynamical system. Coupling is the mutual dependence of the dynamics at spatially separated locations; how the dynamics at one location influences that at another will depend on the system (for discussions on newly-proposed coupling measures see §3). When coupling is strong over large distances (compared to the characteristic lengthscale), the flow is said to be spatially coupled. In contrast, when the dynamics at two locations evolve independent of each other, i.e. the coupling distance is comparable to or less than the characteristic lengthscale, there is no spatial coupling. For open flows, spatial coupling means that the initiation and evolution of local instabilities at distant locations depend on each other rather than on external perturbations; i.e. the coupling is intrinsic. In the mixing layer (studied here), coupling occurs through advection of linear (Kelvin–Helmholtz) and successive nonlinear (subharmonic resonance) disturbances together with upstream propagating feedback from vortex pairings (to the flow origin), which excites subsequent instabilities (this is discussed further in §2); of course, for intrinsic dynamics, the feedback must override the influence of background disturbances at the origin (point of receptivity). A decrease in the amplitude of feedback perturbations will allow the instabilities to be driven by noise (i.e. extrinsic dynamics) and hence result in the loss of spatial coupling. As a result of spatial coupling, the effects of several instabilities can be sensed at any location; i.e. the flow can be described using information from a single probe independent of the location. Thus, one can employ the temporal DS approach. While the lack of spatial coupling renders such a description useless, no simple approach to describe the resulting spatiotemporal dynamics is evident yet. As discussed before, open flows involving different types of local instability cannot be studied using the

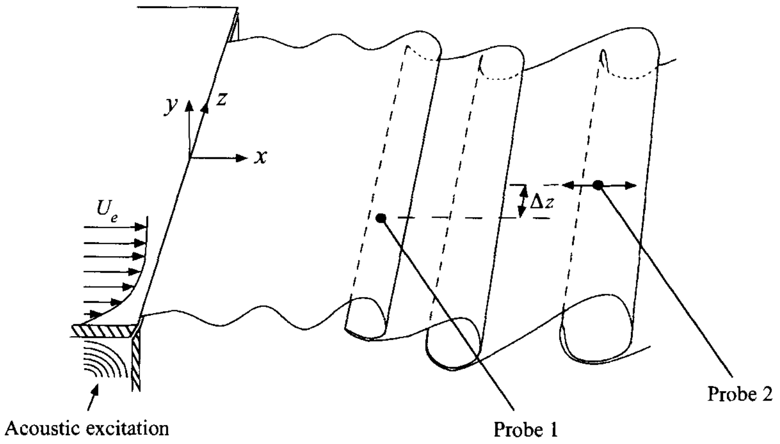

FIGURE 1. Schematic of a plane mixing layer showing the coordinate system and the excitation method; the two probes are separated by Δz to minimize interference.

concept of global instabilities. We overcome this limitation and provide an experimentally verifiable approach for describing low-dimensional dynamics in a wider range of open flows.

The present experimental study aims: (i) to describe intrinsic low-dimensional dynamics in a prototypical open flow, and (ii) to analyse its spatiotemporal dynamics, in terms of the physical-space vortex dynamics, without necessitating full flow field velocity data. For this, we propose to combine temporal DS analyses with spatial measurements (of coherence and cross-bicoherence).

The paper is organized as follows. In §2, low-dimensional dynamics in the control parameter space (frequency and forcing amplitude) are described and depicted in a phase diagram, transitions between dynamical states are discussed, and evidence of dominant feedback is provided. Two distinct, periodic and chaotic, states are studied in further detail since they cover a major portion of the phase diagram. The unforced flow in the low-noise, anechoic environment is also examined briefly as a reference state. In §3 and §4, current methods to study spatiotemporal dynamics are surveyed, the need for new spatial measures is established, and coherence and cross-bicoherence are proposed as appropriate measures of coupling (instead of correlation, used conventionally). These measures are used to determine the spatial extents over which the periodic and chaotic dynamics are representative of the flow, and to detect spatiotemporal dynamics. To examine the effect of spatial coupling on invariant measures of temporal attractors in the flow, the spatial development of the dimension and the largest Lyapunov exponent for the periodic and the chaotic states is discussed in §5. Concluding remarks are presented in §6.

The experiments were performed in a carefully documented, quiet (free-stream turbulence intensity $u'/U_e \leqslant 0.1\%$), initially laminar, plane ML facility in the anechoic chamber at the University of Houston Aerodynamics and Turbulence Laboratory. The flow studied is schematically shown in figure 1, and the facility details are documented in Appendix A. Single-frequency forcing (at 312 Hz) was provided (acoustically) at the ML lip and was chosen from a band of frequencies supported by the excitation chamber (see transfer function in figure 22).

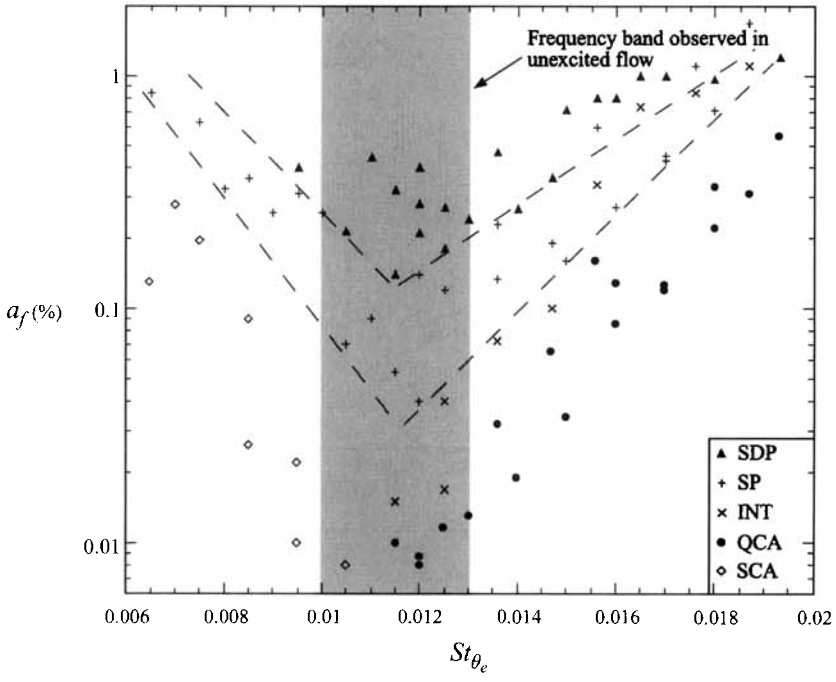

FIGURE 2. Phase diagram for the forced mixing layer. The dashed lines roughly indicate the boundaries for the onset of SP and SDP; note that minimum a_f is required to achieve SP and SDP at $St_{\theta_e} \approx 0.0115$. The shading denotes the frequency band observed in the unforced flow.

2. Temporal dynamics of the mixing layer

2.1. *The phase diagram*

Convectively unstable local dynamics in the ML involve vortex roll-up and pairings of these vortices. We chose a measurement location ($x \approx 130\ \theta_e$) where the probe senses footprints of all important events: roll-up ($x \approx 50$–$60\ \theta_e$), first pairing ($x \approx 110$–$130\ \theta_e$) and second pairing ($x \approx 200$–$220\ \theta_e$); note that the precise roll-up and pairing locations depend upon the forcing frequency and amplitude, which control the growth rate and saturation location of the unstable modes. The probe's transverse location corresponds to $U(y)/U_e \approx 98\%$, where a clear imprint of large-scale events is obtained but effects due to small scales or internal vorticity laminations (within a vortex) are essentially avoided; a long-prong single-wire probe was used to avoid probe-induced shear layer tone (Hussain & Zaman 1978). The control parameters used are: the Strouhal number $St_{\theta_e} (\equiv f_{ex}\theta_e/U_e$, U_e = exit velocity and f_{ex} = excitation frequency) and the non-dimensional forcing amplitude $a_f (\equiv u'_f/U_e$, the normalized peak r.m.s.-velocity fluctuation at f_{ex} recorded near the ML origin, $x/\theta_e \approx 4$); U_e was varied to change St_{θ_e} in the linear instability range predicted by Michalke (1965). Velocity signals were analysed for the ranges: $0.008\% \leqslant a_f \leqslant 1\%$ and $0.006 \leqslant St_{\theta_e} \leqslant 0.02$. We use mutual information (MI), phase portraits, Poincaré sections, correlation dimension ν and largest Lyapunov exponent λ (in bits per orbit (b.p.o.), normalized by the subharmonic period) to describe temporal attractors. All Poincaré sections show both positive and negative crossings on a plane inclined at 45° to the $[u(t), u(t+\tau)]$ phase space axes. Computations of the invariant measures are briefly described in Appendix B.

The periodic state, stable double pairing (SDP), is found at all St_{θ_e} studied, for sufficiently high a_f (see figure 2). At low a_f, two chaotic states, the quarterharmonic

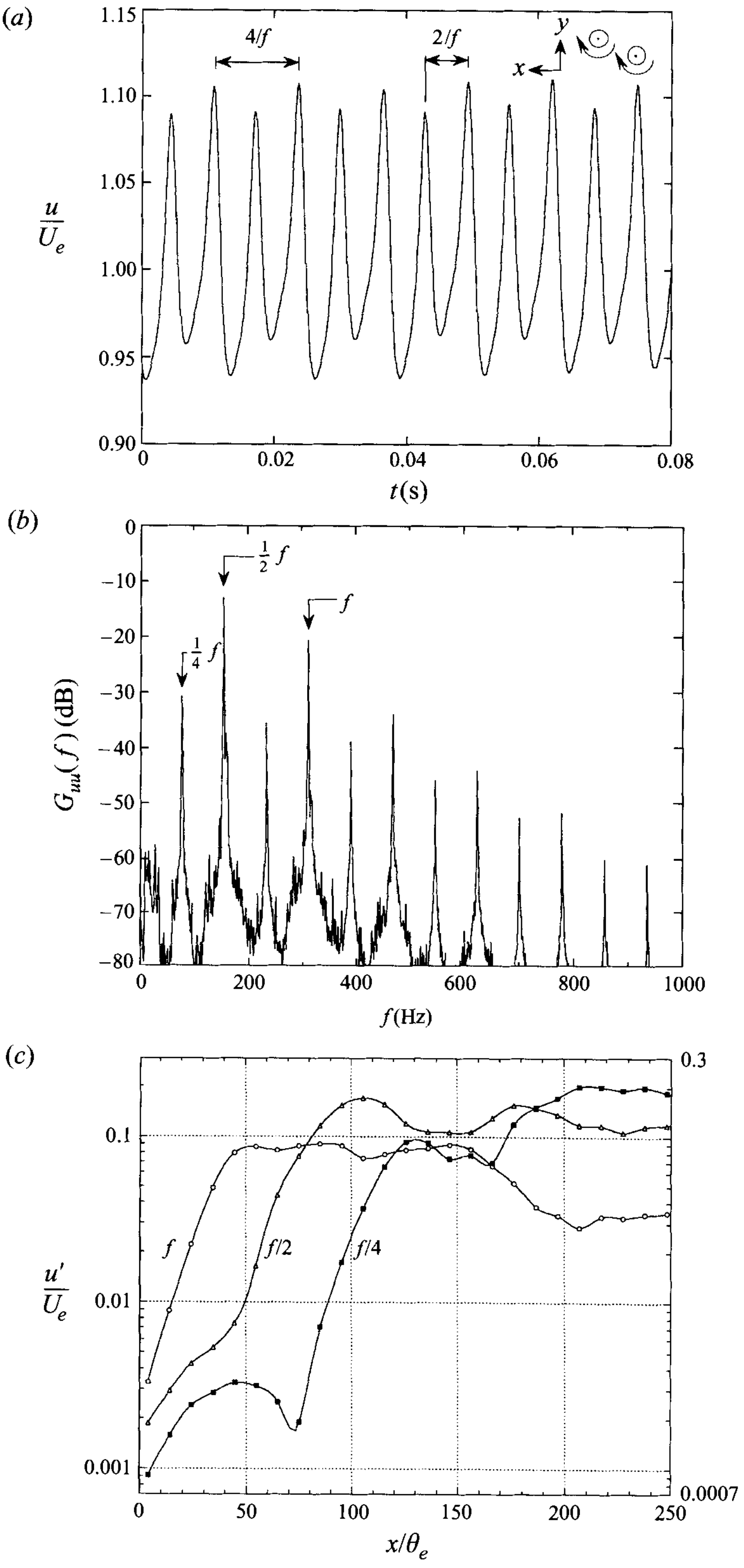

FIGURE 3. For caption see facing page.

chaotic attractor (QCA) and the subharmonic chaotic attractor (SCA), are found for two different ranges of St_{θ_e} (above and below 0.0115, respectively). For intermediate a_f, the stable pairing (SP) attractor is found with periodic/chaotic dynamics (discussed in §2.1.2). Interestingly, at $St_{\theta_e} \approx 0.0115$, the a_f required to achieve SP and SDP has a minimum (this supportive evidence of feedback will be discussed in §2.3); the shaded area in figure 2 denotes the dominant instability frequency band ($0.01 \leqslant St_{\theta_e} \leqslant 0.013$) in an unforced ML (discussed in §2.3). Since the dynamics is periodic at high a_f and becomes chaotic with decreasing a_f, we describe these states as they occur for decreasing a_f and then analyse the transitions between them.

2.1.1. *SDP*

This state occurs for relatively high excitation amplitudes, $0.15\% \leqslant a_f$ (see figure 2); note that *only* the fundamental instability is forced. The vortex dynamics involve forced periodic roll-up and self-excited periodic first pairing (of rolled-up vortices) and second pairing (of once-paired vortices); pairing phenomena have been studied previously (Winant & Browand 1974; Zaman & Hussain 1980). These events result in spectral peaks (figure 3*b*) at the fundamental f, the subharmonic $\frac{1}{2}f$ and the quarterharmonic $\frac{1}{4}f$; even $\frac{1}{8}f$, indicating third pairing, is detected farther downstream. Proximity of the probe to the first pairing location results in a higher subharmonic amplitude than that of the quarterharmonic or the fundamental, as is also evident from the time trace (figure 3*a*) which has a dominant subharmonic period. The subharmonic has a broader spectral base than the quarterharmonic, indicating slight subharmonic phase jitter (jitter refers to variations in the instantaneous phase at a fixed x); quarterharmonic phase jitter also results in a similar broadening of the quarterharmonic in a spectrum recorded farther downstream. Alternating peak values in the time trace suggest transverse displacement of vortex centres (see inset of figure 3*a*), indicating initiation of the second pairing.

The streamwise evolutions of peak amplitudes of significant frequencies ($f, \frac{1}{2}f, \frac{1}{4}f$) in the SDP spectrum are shown in figure 3(*c*). The exponential growth at all frequencies for $x/\theta_e < 40$ is followed by fundamental saturation, causing roll-up, at $x/\theta_e \approx 50$ and a concomitant increase in the subharmonic growth rate due to nonlinear interactions with the fundamental (the subharmonic resonance phenomenon; see Kelly 1967). The resonance results in the first pairing by $x/\theta_e \approx 110$, inferred from the subharmonic saturation. Meanwhile, the quarterharmonic growth rate is modified owing to a similar resonance with the subharmonic. In the region $130 \leqslant x/\theta_e \leqslant 170$, the quarterharmonic growth suppression appears to be due to local quarterharmonic phase jitter. The configuration of pairing vortices (which governs the instantaneous quarterharmonic phase at a given x) during the second pairing is extremely sensitive to ambient perturbations, making it impossible to maintain precisely the same configuration (i.e. the same phase) at a given x during each pairing; consequently, the second pairing process is not perfectly periodic. However, farther downstream (when vortices nearly complete pairing) this sensitivity is of little consequence, and resonant quarterharmonic growth resumes and culminates in a complete second pairing by $x/\theta_e \approx 220$. That is, the growth rate is most sensitive to phase during pairing than it is before or after, and

FIGURE 3. For SDP: (*a*) the time trace recorded at $x/\theta_e \approx 120$ and $U(y)/U_e \approx 98\%$, for $a_f \approx 0.2\%$ and $St_{\theta_e} \approx 0.012$, displays the dominance of the subharmonic $\frac{1}{2}f$ and the quarterharmonic $\frac{1}{4}f$; the relative transverse displacement of pairing vortices is also sketched; (*b*) the power spectrum shows peaks at f (due to roll-up), $\frac{1}{2}f$ (due to the first pairing) and $\frac{1}{4}f$ (due to the second pairing); and (*c*) the streamwise evolutions of peak-amplitudes at f, $\frac{1}{2}f$ and $\frac{1}{4}f$ indicate complete vortex roll-up by $x/\theta_e \approx 55$, complete first pairing by $x/\theta_e \approx 110$, and complete second pairing by $x/\theta_e \approx 220$.

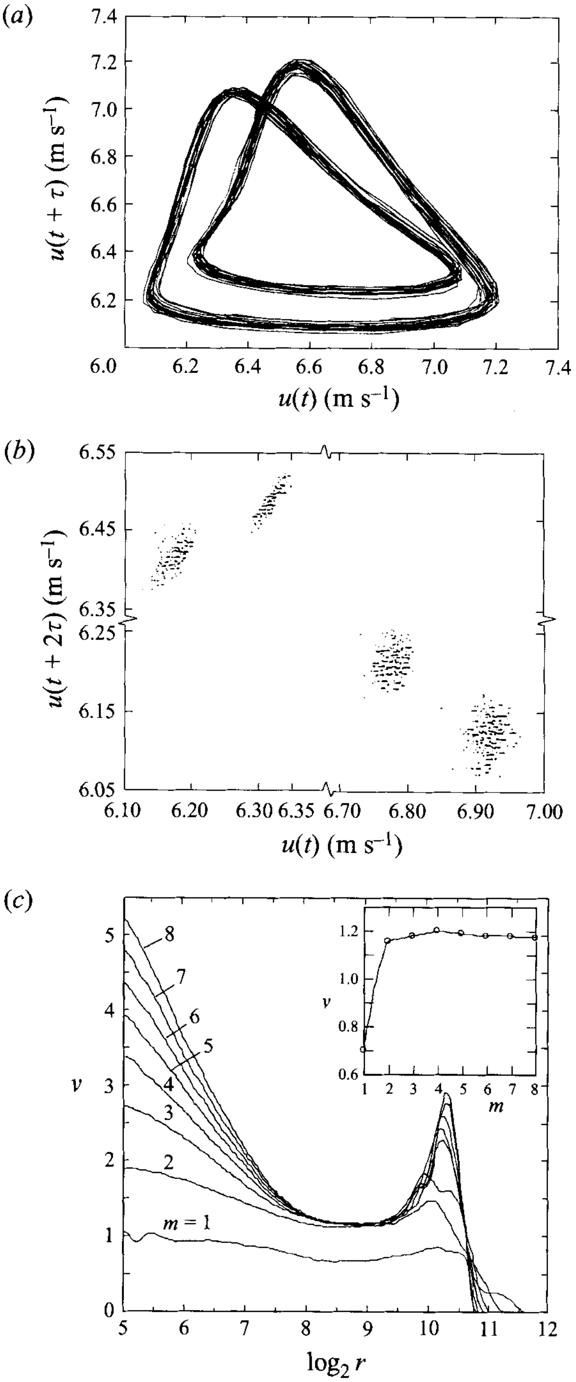

FIGURE 4. For SDP: (*a*) the phase portrait shows the period-2 limit cycle; (*b*) magnified view of the Poincaré section shows four distinct clusters corresponding to crossings of the limit cycle; and (*c*) correlation dimension ν as a function of distance r in phase-space for different embedding dimensions m shows good convergence for ν at $m = 3$ (see inset).

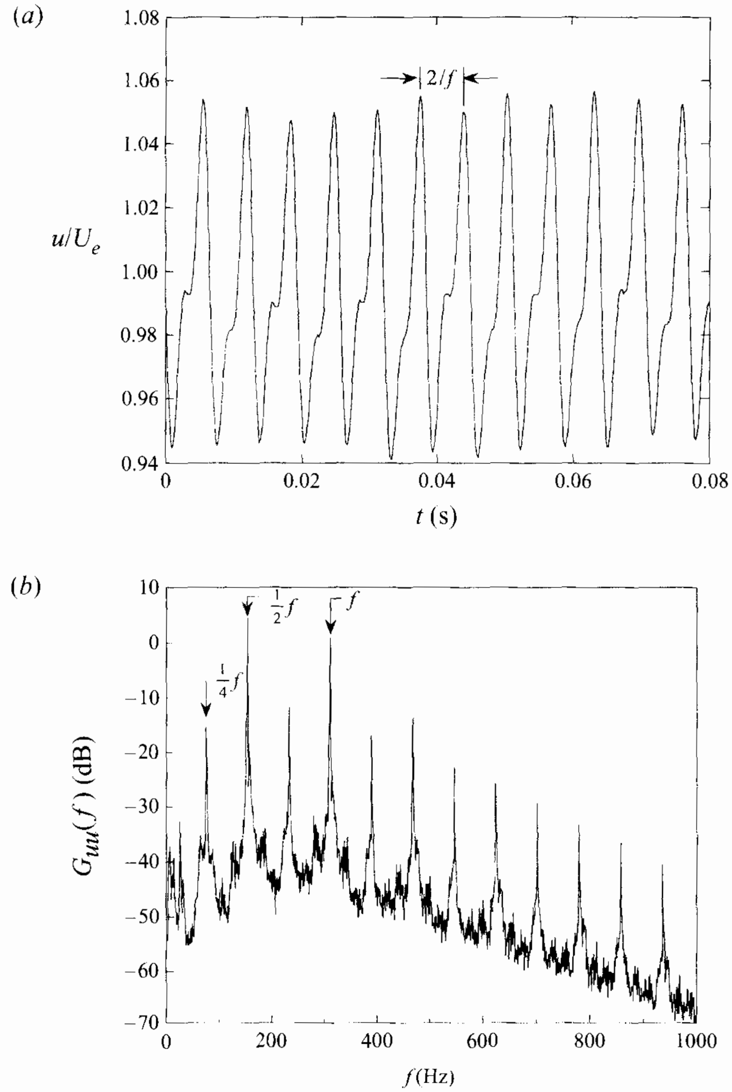

FIGURE 5. For SP: (*a*) time trace at $x/\theta_e \approx 120$ and $U(y)/U_e \approx 98\%$, for $a_f \approx 0.04\%$ and $St_{\theta_e} \approx 0.012$, shows dominance of the subharmonic and an aperiodic quarterharmonic; and (*b*) the power spectrum shows fundamental f, subharmonic $\frac{1}{2}f$ and quarterharmonic $\frac{1}{4}f$ peaks on a broadband pedestal, suggesting chaotic modulations.

even forcing at high a_f cannot eliminate the jitter; this jitter will be analysed further in §§3.2.1, 4.1 and 5.1.

The phase portrait (figure 4*a*) is obtained using time-delayed reconstruction with a delay corresponding to the first minimum of the MI (Fraser & Swinney 1986). The period-2 limit cycle has scatter that can be attributed to slight changes in successive pairing locations causing weak modulations of the subharmonic/quarterharmonic. The Poincaré section for SDP (magnified in figure 4*b*) has clusters separated by at least 0.6 m s^{-1} (much larger than the maximum scatter, which is within 0.08 m s^{-1}), indicating limit cycle behaviour at large phase-space scales. Note that the magnified view of the clusters reveals no pattern, suggesting that the limit cycle is noise-contaminated. Estimates of correlation dimension, $\nu \approx 1.18$ (embedding dimension

$m = 3$) and largest Lyapunov exponent, $\lambda \approx 0$ b.p.o., confirm periodicity of the flow. Figure 4(c) shows $\mathrm{d}\log_2 C(r)/\mathrm{d}\log_2 r\,(\equiv \nu)$ as a function of the scale ($\log_2 r$) for various embedding dimensions ($m \leqslant 8$); moderate scaling region ($r_{max}/r_{min} \approx 4$–6) and good convergence (see inset) confirm that SDP is a periodic attractor.

2.1.2. *SP*

At a fixed St_{θ_e}, as a_f is reduced, the roll-up location and hence the pairing locations move farther downstream, since the instability waves travel farther before achieving the saturation amplitude (Freymuth 1966). Thus, feedback (i.e. the induced velocity fluctuation at the origin from paired structures) from the first and second pairings becomes weaker (than for SDP); more importantly, the second pairing becomes phase-unlocked (i.e. feedback phase at the origin varies from one pairing to the next). Consequently, the second pairing ceases to be periodic and its location shifts (inferred from a broadband quarterharmonic in a downstream spectrum, not shown). However, the relatively periodic subharmonic in the time trace (figure 5a, with $a_f \approx 0.04\,\%$ and $St_{\theta_e} \approx 0.012$) indicates a stable first pairing. The spectral filling in figure 5(b), with discrete frequencies on a broadband pedestal, indicating modulations of the subharmonic/quarterharmonic (see also the time trace), suggests chaotic dynamics and is discussed below.

The phase portrait and Poincaré section (figures 6a, b) indicate an increased spread in the trajectories with only three distinct clusters as opposed to four for SDP; the spread (≈ 0.2 m s^{-1}) is comparable to the cluster separation (≈ 0.35 m s^{-1}). We find two scaling regions from dimension calculations (see figure 6c): $\nu \approx 1.3$ with a negative $\lambda\,(\approx -0.038$ b.p.o.) at large phase-space scales, and $\nu = 1.9$–1.95 with a positive $\lambda\,(\approx 0.045$ b.p.o.) at small phase-space scales; λ computations are explained in Appendix B. Broze's (1992) analysis of noise-contaminated sinusoidal signals also yielded $\lambda < 0$ and $1 < \nu < 2$, suggesting that the algorithms used to compute ν and λ are sensitive to noisy data and provide averaged estimates (between high-dimensional (due to aperiodic modulations) and periodic dynamics). However, $\nu \approx 2$ and $\lambda > 0$ at small phase-space scales suggest chaotic dynamics. The large scales in phase space correspond to the nearly periodic first pairing dynamics, while the behaviour at small scales reflects the changes in the details (phase modulations) of the (first and second) pairing processes. At this stage, the SP attractor is best characterized as a noisy limit cycle when viewed at large scales, with deterministic chaos at small scales.

2.1.3. *Chaotic modulations*

As a_f is decreased from that required for SP, two different chaotic states occur for $St_{\theta_e} \geqslant 0.012$ (QCA) and $St_{\theta_e} < 0.012$ (SCA) (see figure 2).

QCA: A representative signal and spectrum of the chaotic state for $a_f \approx 0.12\,\%$, $St_{\theta_e} \approx 0.017$ are shown in figure 7(a, b). The spectrum has sharp sidebands around the subharmonic (marked with a dashed line) indicating nearly periodic modulations of the first pairing, owing to nearly periodic shifts in the pairing locations upstream and downstream (caused by periodic changes in the feedback phase), and a broadband quarterharmonic indicating chaotic shifts in the second pairing location; amplitude modulations in the time trace reflect variations in the induced velocity from pairing or once-paired vortices.

Streamwise growths of peak amplitudes of the fundamental f, the higher and lower sidebands (f_h, f_l) of the subharmonic and the quarterharmonic $\frac{1}{4}f$ are shown in figure 7(c). The fundamental grows exponentially and saturates after $x/\theta_e \approx 55$, where roll-up occurs. The sidebands' growth and then their saturation in the region $x/\theta_e \approx 90$–110

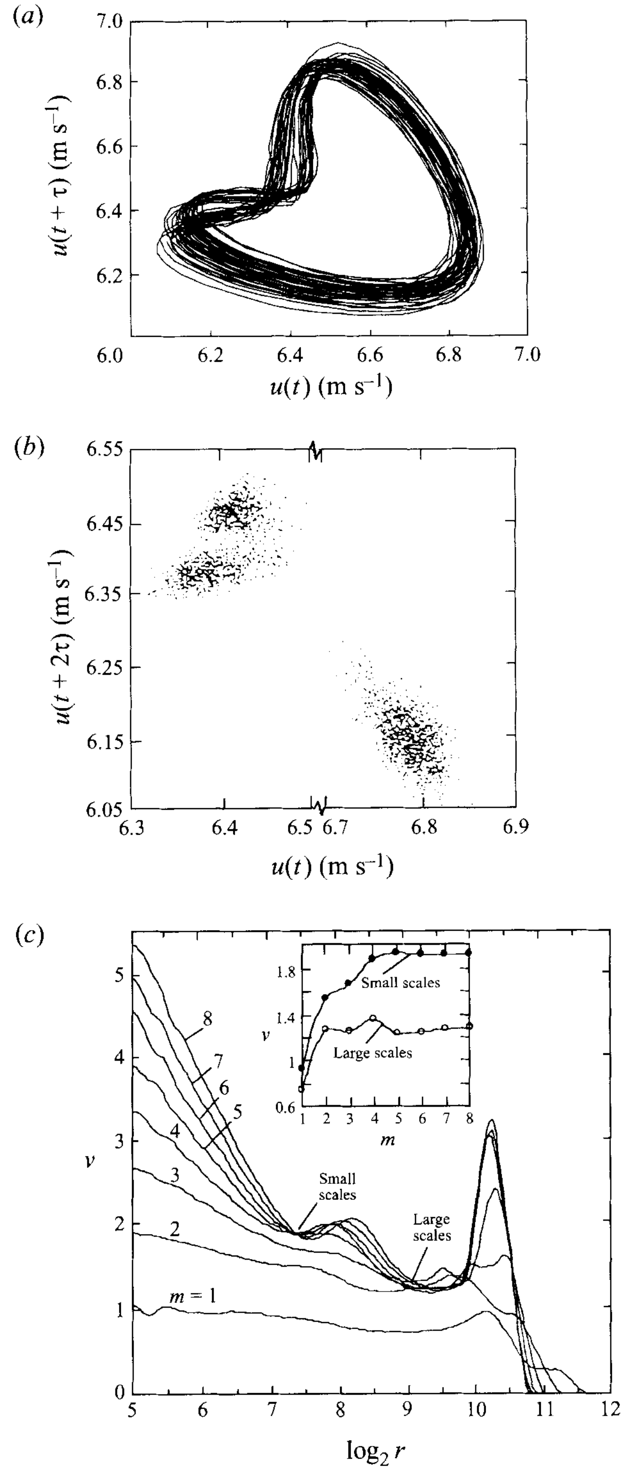

FIGURE 6. For SP: (*a*) phase portrait shows larger spread of trajectories suggesting a noisy limit cycle; (*b*) magnified view of Poincaré section displays three smeared out clusters; and (*c*) correlation dimension ν versus phase-space distance r at different embedding dimensions m displays two distinct scaling regions with $\nu \approx 1.3$ and $\nu \approx 1.9$–1.95.

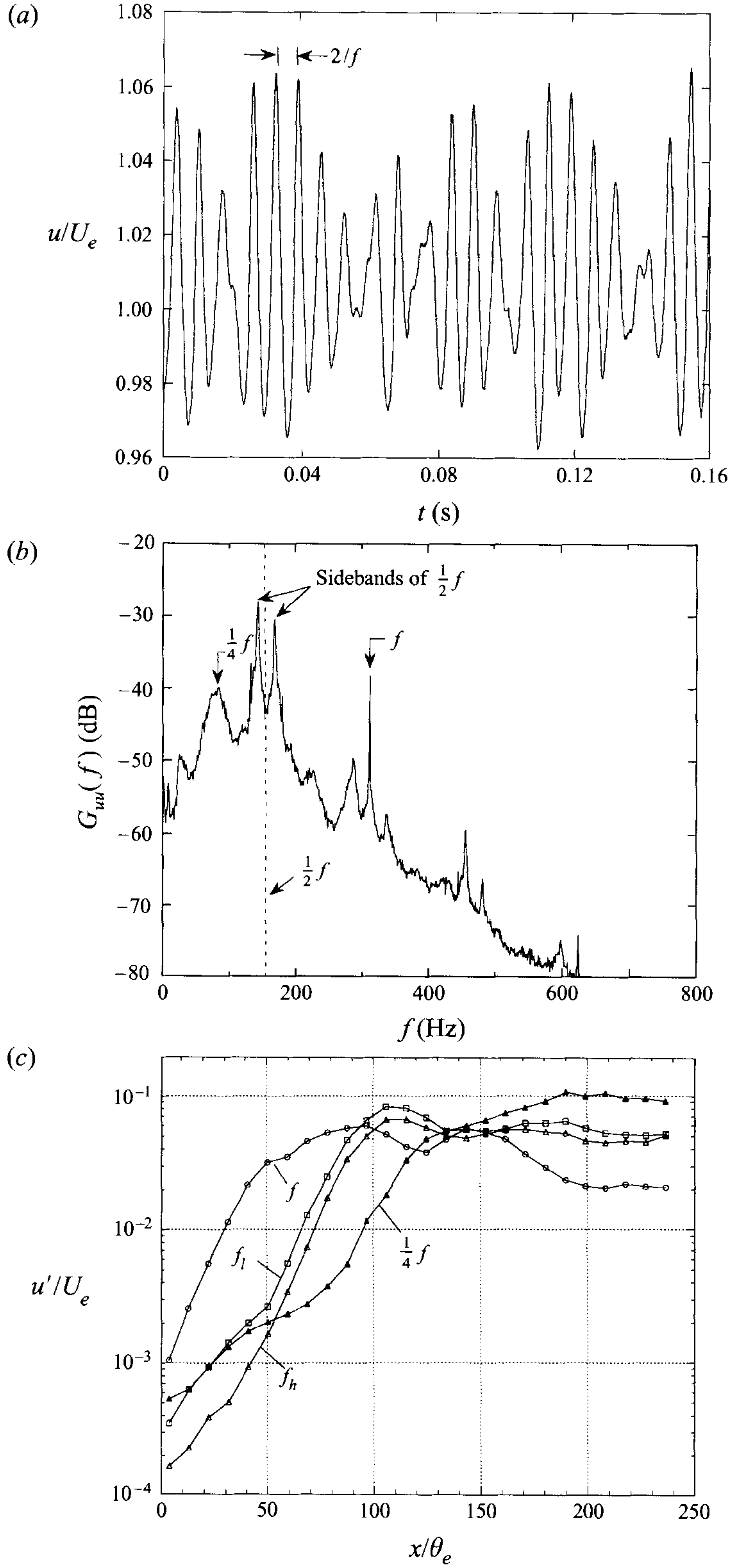

FIGURE 7. For caption see facing page.

indicate a modulated first pairing. Fluctuations in the quarterharmonic growth for $110 \leqslant x/\theta_e \leqslant 200$ are a result of its chaotically varying phase, which in the initial stages of the resonance determines the modified quarterharmonic growth rate (Monkewitz 1988). Nevertheless, the enhanced quarterharmonic growth rate during the sidebands' saturation (beyond $x/\theta_e \approx 90$) indicates the second subharmonic resonance. The quarterharmonic saturation location is not clearly defined owing to chaotic shifting of the second pairing over a sizeable flow region.

The phase portrait, shown in figure 8(*a*), and the absence of tight and well-separated clusters in its Poincaré section (figure 8*b*) are expected for this chaotic attractor. Dimension calculations revealed $\nu \approx 2.43$ ($m = 4$), reasonable scaling region (factor of 2–4) and convergence (see figure 8*c*). The largest Lyapunov exponent is positive ($\lambda \approx 0.32$ b.p.o.), indicating chaos.

The method of surrogate data (Theiler *et al.* 1992) provides a means to differentiate nonlinearity from linearly correlated noise in experimental data (briefly described in Appendix B) and has been used in well-known examples of low-dimensional chaos (e.g. in Rayleigh–Bénard convection); we applied this method to QCA. If a dynamical invariant measure computed from surrogate data (generated by scrambling the phase of the original data while preserving its Fourier amplitudes) is the same as that obtained from the original data, then the original process is a linear stochastic process; if the measure is different the original process is nonlinear. Figure 8(*d*) shows ν for the surrogate data. The absence of convergence or scaling region shows that the data represents a nonlinear process. Note that while this observation is not a proof of chaotic dynamics, it establishes the fact that the dynamics detected is intrinsically nonlinear. Since $\nu \approx 2.3$–2.6 and $\lambda > 0$, the data reflects low-dimensional chaos.

SCA: A different type of chaotic state is found for $St_{\theta_e} < 0.012$, whose spectrum is depicted in figure 9(*a*) for $a_f \approx 0.022\,\%$ and $St_{\theta_e} \approx 0.0095$. Unlike that for QCA, this spectrum has very little quarterharmonic content; a broadband subharmonic indicates aperiodic modulations of the first pairing. Calculations of ν(≈ 2.2, see figure 9*b*) and λ(≈ 0.09 b.p.o.) indicate chaotic behaviour. Since we are interested in the ML dynamics that includes the second pairing and SCA involves low-dimensional dynamics of only the first pairing, we do not focus on SCA further. For the same reason, we focus on SDP and not on SP.

2.1.4. *Low-amplitude states*

As a_f is reduced further (below that for the chaotic states), the subharmonic also becomes weaker, and the broadband spectral content increases. Time series of these low-amplitude (forced) states and of the unforced state (i.e. without periodic forcing) yielded no scaling regions and little or no convergence (for $m \leqslant 8$ and 200000 data points) in dimension calculations, implying that, if the dynamics is indeed deterministic, it could be high-dimensional or that single-point measurements are inadequate.

In summary, most states identified in the flow are characterized by low-dimensional attractors and correspond to quite different vortex roll-up and pairing dynamics which are periodic and chaotic. In the following we examine the transitions between various states for three a_f ranges.

FIGURE 7. For QCA: (*a*) time trace at $x/\theta_e \approx 120$ and $U(y)/U_e \approx 98\,\%$, for $a_f \approx 0.12\,\%$ and $St_{\theta_e} \approx 0.017$, shows amplitude modulations of the subharmonic with occasional quarterharmonic; (*b*) the power spectrum has peaks at the fundamental f and sidebands (f_l, f_h) around the subharmonic (denoted by a dashed line), and a broadband quarterharmonic $\frac{1}{4}f$; and (*c*) the streamwise evolutions of peaks of the r.m.s.-velocity fluctuation profiles for f, f_l, f_h and $\frac{1}{4}f$ reflect completed vortex roll-up by $x/\theta_e \approx 60$, first pairing for $80 \leqslant x/\theta_e \leqslant 120$, and second pairing for $x/\theta_e \geqslant 180$.

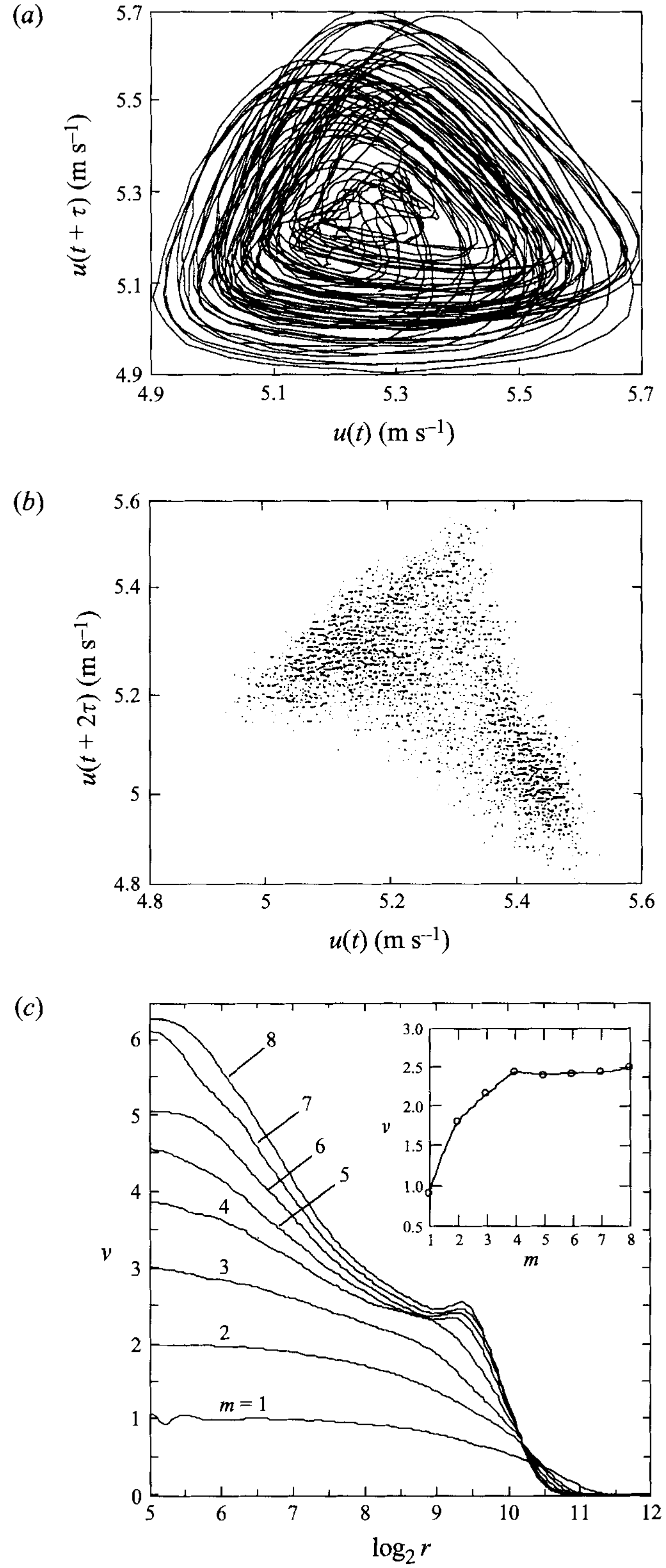

FIGURE 8(*a–c*). For caption see facing page.

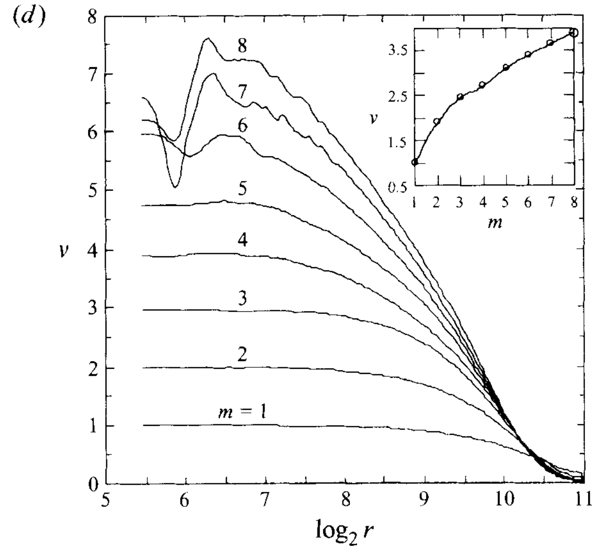

FIGURE 8. For QCA: (*a*) the phase portrait shows a two-dimensional projection of the strange attractor; (*b*) the Poincaré section has no separated clusters as observed for the periodic attractors; and (*c*) the correlation dimension ν is shown as a function of distance r in phase-space at different embedding dimensions m. (*d*) Correlation dimension ν at different embedding dimensions m for the surrogate data shows that ν does not converge for $m \leqslant 8$ (see inset).

2.2. *Transitions in the phase diagram*

At high forcing amplitudes, as a_f is increased (for a fixed St_{θ_e}) from that required for SP, a new state (SDP) appears with a stable quarterharmonic in addition to an already stable subharmonic (see figure 2). Thus, increasing a_f produces increased spatial order in that (additional) pairings farther downstream become periodic; higher a_f causes earlier roll-up and pairing, whose stronger, phase-locked feedback excites and sustains the periodicity. For a_f higher than that required for SDP, an $\frac{1}{8}f$ peak (i.e. a third pairing) also appears. In the low a_f range, increasing a_f produces an apparent intermittency transition from QCA to SP during which the nearly periodically modulated first pairing becomes periodic. The intermittent behaviour is evident in the signal during this transition, which comprises periodic segments interspersed with chaotic ones (see figure 10). Physically, the flow switches between pairing periodically (when the subharmonic is nearly phase-locked and its saturation location is fixed) and chaotically (when the subharmonic phase becomes unlocked and its saturation location shifts). A similar intermittency transition was recently investigated in a forced jet (Broze & Hussain 1996). Another interesting transition was detected from the unforced ML (denoted as UML) to QCA and is described below.

The UML spectrum (see figure 11(*a*), recorded at $x/\theta_e \approx 150$) has a broadband fundamental centred at $St_{\theta_e} \approx 0.01$, and a broadband subharmonic around $St_{\theta_e} \approx 0.005$. A spectral array is shown in figure 11(*b*) for $0 \leqslant a_f \leqslant 0.38\%$ and $St_{\theta_e} \approx 0.0165$ recorded at $x/\theta_e \approx 140$. The frontmost spectrum corresponds to UML ($a_f \approx 0$), and has a broadband fundamental (f_{unf}, with $St_{\theta_e} \approx 0.01$) and a broadband subharmonic (around $St_{\theta_e} \approx 0.005$) owing to aperiodic roll-up and first pairing, respectively. The sequence of events that leads to QCA for increasing a_f can be described in two stages. The first stage (s1–s3 in figure 11*b*) involves nonlinear interactions of the excited frequency f with the peak of the broadband around $St_{\theta_e} \approx 0.01$ to produce the sum $f+f_{unf}$ ($St_{\theta_e} \approx 0.0265$) and the difference

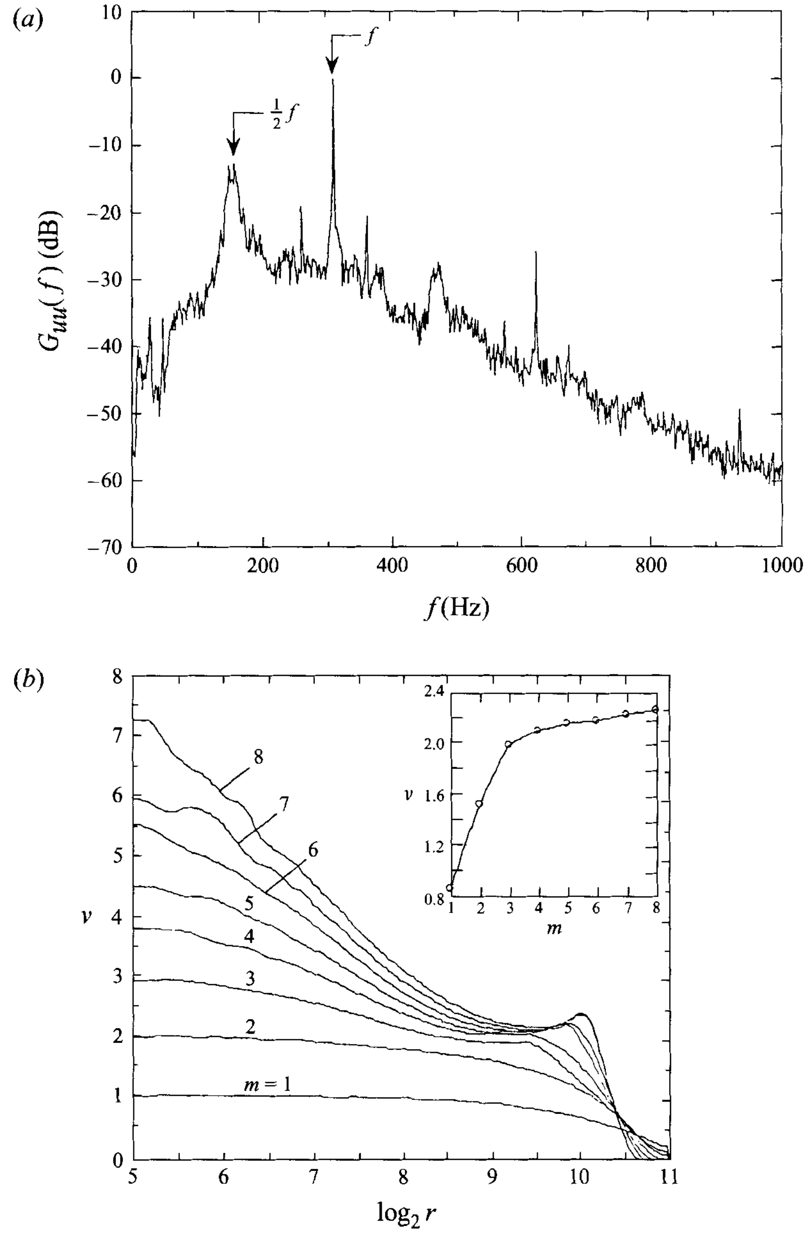

FIGURE 9. For SCA: (*a*) the power spectrum at $x/\theta_e \approx 140$ and $U(y)/U_e \approx 98\,\%$, for $a_f \approx 0.022\,\%$ and $St_{\theta_e} \approx 0.0095$, has a fundamental f peak and a broadband subharmonic; and (*b*) the correlation dimension ν for different distances r in phase-space is shown for various embedding dimensions m.

$f - f_{unf} (= f_l, St_{\theta_e} \approx 0.0065)$ frequencies; f_h (belonging to the broadband of f_{unf}) and f_l (see in s3) bracket the subharmonic ($\frac{1}{2}f$, $St_{\theta_e} \approx 0.0082$). (Note that in s8, f_l and f_h correspond to $St_{\theta_e} \approx 0.0076$ and 0.0089, respectively.)

In the second stage (s4–s8 in figure 11*b*), for increasing a_f, the peaks at f_l and f_h move closer together (i.e. $f_h - f_l$ decreases) and become dominant compared to the background, and finally QCA is obtained (see s8). Note the disappearance of the broadband around $\frac{1}{2}f_{unf}$ and the emergence of a broadband quarterharmonic ($\frac{1}{4}f$, $St_{\theta_e} \approx 0.0041$). We term

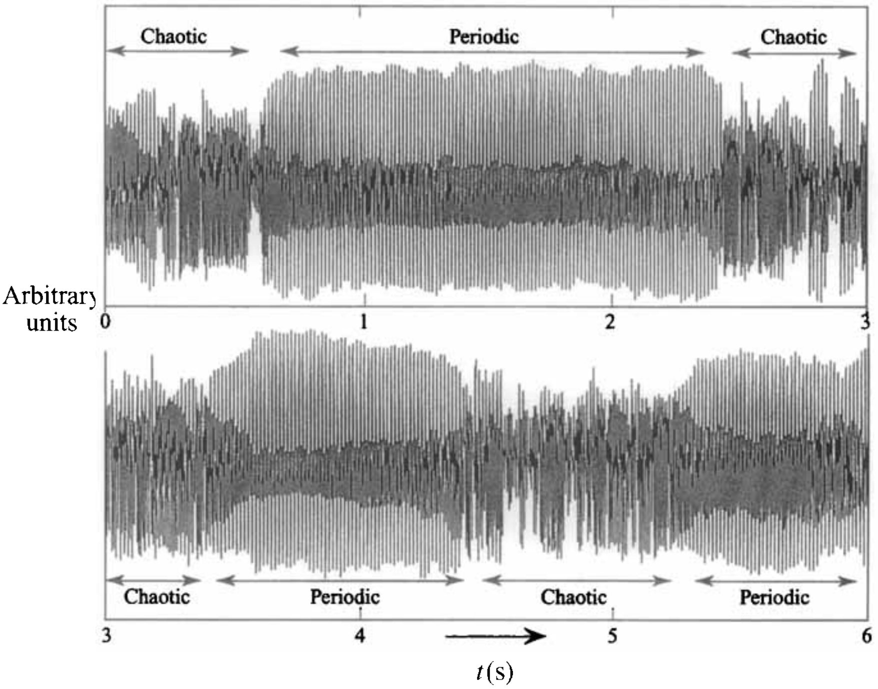

FIGURE 10. Time trace recorded at $x/\theta_e \approx 140$ and $U(y)/U_e \approx 98\,\%$, for $a_f \approx 0.74\,\%$ and $St_{\theta_e} \approx 0.0165$, shows simultaneous presence of periodic and chaotic behaviour, indicating intermittency.

the process of shifting of the sidebands by varying a_f to be 'natural detuning'. Further increase in a_f produces SP (when f_l and f_h merge, see figure 5*b*). This process contrasts with the theoretically (Monkewitz 1988) and experimentally (Husain & Hussain 1989) studied phenomenon where detuning results from forcing provided simultaneously at f and at $(\frac{1}{2}f-\Delta f)$ (i.e. detuning is controlled by changing Δf); in our case, Δf is chosen (depending on a_f and St_{θ_e}) by the flow. The shifting of the pairing location in x causes the instantaneous subharmonic phase at an upstream location to vary (hence giving rise to a Δf). Such pairings provide feedback to the origin at varying intervals causing ϕ_s (the subharmonic feedback phase at the origin) to change. The sidebands' approach toward each other (i.e. decreasing Δf) with increasing a_f implies smaller changes in ϕ_s between successive pairings, i.e. near phase-locking. Stronger sidebands indicate that pairing occurs progressively further upstream. Eventually, the emergence of a distinct subharmonic (when f_l and f_h merge) signifies phase-locking (constant ϕ_s); thus, subharmonic saturation (and hence pairing) always occurs at the same x (i.e. SP occurs).

2.3. *Feedback-driven dynamics*

In this section we argue for the existence of feedback and provide experimental evidence to support it. Several experimental investigations, including Zaman & Hussain (1980) and the present one, show that, for an unforced ML, roll-up occurs in a broadband around $St_{\theta_e} \approx 0.012$ (see figure 11*a*), even though $St_{\theta_e} \approx 0.017$ has the highest growth rate according to spatial linear stability analysis (Michalke 1965; also experiments of Freymuth 1966). An explanation for this documented preference was proposed (in terms of induced velocity fields of vortices) to be the result of the strongest feedback at $St_{\theta_e} \approx 0.012$ (Hussain *et al.* 1986).

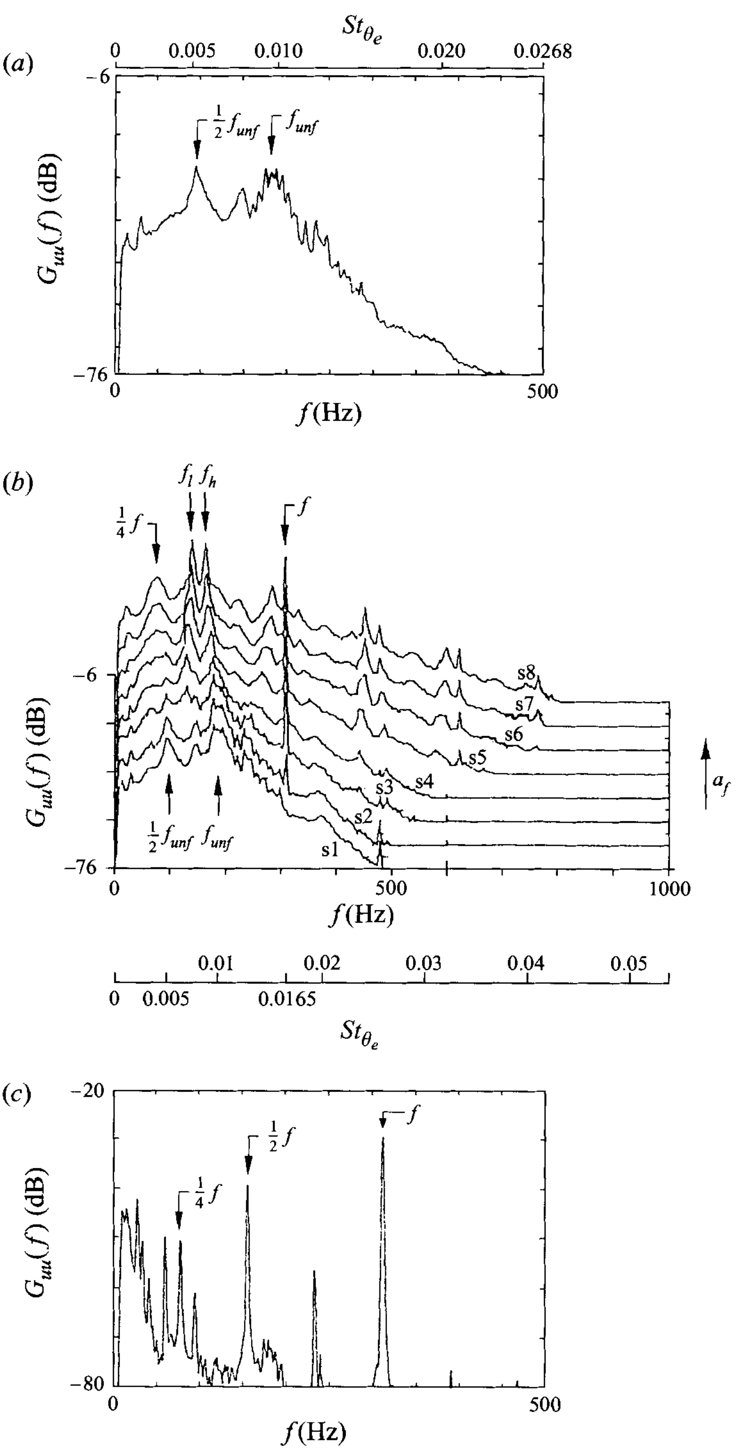

FIGURE 11. (*a*) Power spectrum for the unforced ML recorded at $x/\theta_e \approx 150$ has a broadband fundamental at $St_{\theta_e} \approx 0.01$, and a broadband subharmonic at $St_{\theta_e} \approx 0.0055$. (*b*) Spectral array for transition to QCA from UML with $0 \leqslant a_f \leqslant 0.038\,\%$, shows the emergence of the lower subharmonic sideband f_l (at s3) followed by progressive shifting (after s4) of the sidebands (f_l,f_h) toward each other. (*c*) Power spectrum for SDP recorded close to the ML origin, at $x/\theta_e \approx 4$, indicates dominant fundamental f due to forcing, and subharmonic $\frac{1}{2}f$ and quarterharmonic $\frac{1}{4}f$ peaks due to feedback.

Feedback from the first and second pairings is evidenced from $\frac{1}{2}f$ and $\frac{1}{4}f$ peaks in the SDP spectrum recorded near the ML origin, $x/\theta_e \approx 4$ (see figure 11*c*); a similar spectrum (not shown) with a weaker quarterharmonic is observed for SP. If feedback is responsible for roll-up around $St_{\theta_e} = 0.012$ and pairing around $St_{\theta_e} = 0.006$ in UML (see figure 11*a*), then one would expect that the minimum a_f required to produce SP (periodic roll-up and pairing) is at $St_{\theta_e} \approx 0.012$. This is because feedback from pairing at $\frac{1}{2}f_{ex}$ (subharmonic of the excited frequency) would reinforce the already existing pairing feedback at $\frac{1}{2}f_{unf}$ (subharmonic of the natural roll-up frequency, $St_{\theta_e} \approx 0.011$–$0.013$), both of which belong to the same frequency band around $St_{\theta_e} = 0.006$. Indeed our observations show that the minimum a_f required for SP is at $St_{\theta_e} \approx 0.0115$ (where the wedge-shaped region in figure 2 is centred). When excited at very low a_f and $St_{\theta_e} \neq 0.0115$, to sustain pairing at $\frac{1}{2}f_{ex}$, feedback from this pairing must be stronger than feedback from pairing at $\frac{1}{2}f_{unf}$. When forced at a higher a_f, roll-up and pairing occur earlier in x, thereby inducing stronger feedback (larger vortex-induced velocity fluctuations) at the excited frequency. Thus, for $St_{\theta_e} \neq 0.0115$, substantially higher a_f is required to produce SP and SDP (note the logarithmic ordinate scale in figure 2). Thus, we have seen here evidence of feedback and a self-consistent explanation for the ML phase diagram based on the existence of feedback.

In the next two sections, we propose a set of spatial measures to identify spatiotemporal dynamics in open flows and briefly review previous studies and their limitations. Experiments were conducted for SDP, QCA and UML (to provide us with some understanding of the naturally evolving flow in the low-noise environment of the anechoic chamber). SDP and QCA are chosen instead of SP and SCA, since they involve low-dimensional dynamics of both the first and the second pairing, and cover a wide region of control parameter space.

3. Spatial characteristics

We begin by discussing the critical differences between temporal and spatiotemporal dynamics in a flow. As explained in § 1, spatially separated points in a flow domain are said to be coupled when dynamics at these points depend on each other. Since the temporal dynamics on an attractor at a certain spatial location can be predicted from knowing the evolution on an attractor observed at another location (in a coupled domain), the essential flow dynamics can be considered to be temporal. Note that the two attractors may be quite different in spatially developing flows since different modes can dominate in different flow regions. When coupling is lost the resulting dynamics is spatiotemporal. Thus, 'loss of coupling' implies the unpredictability of dynamics at one point using measurements at another. This loss can come from temporal chaos due to exponential sensitivity to initial conditions. In a spatially developing flow, temporal chaos will also result in spatial disorder (e.g. see Rasmussen & Bohr 1987). Thus, it would be impossible to use finite-precision single-point measurements to predict the dynamics at a later time (at the same spatial location) or at another spatial location; the limits of such predictability in time and space are related to λ (the largest Lyapunov exponent) and the extent of spatial correlation. Since small differences in the initial conditions are amplified in space and time, this is an example of spatiotemporal chaos (in open flows). In this respect, Deissler & Kaneko (1987) defined 'convective chaos' and detected it in a reference frame moving with the convective instabilities in a Ginzburg–Landau equation simulation (an open flow model). Having studied the key features of temporal and spatiotemporal dynamics, we need appropriate measures to identify and describe them. Such measures will dictate the number, spacing and

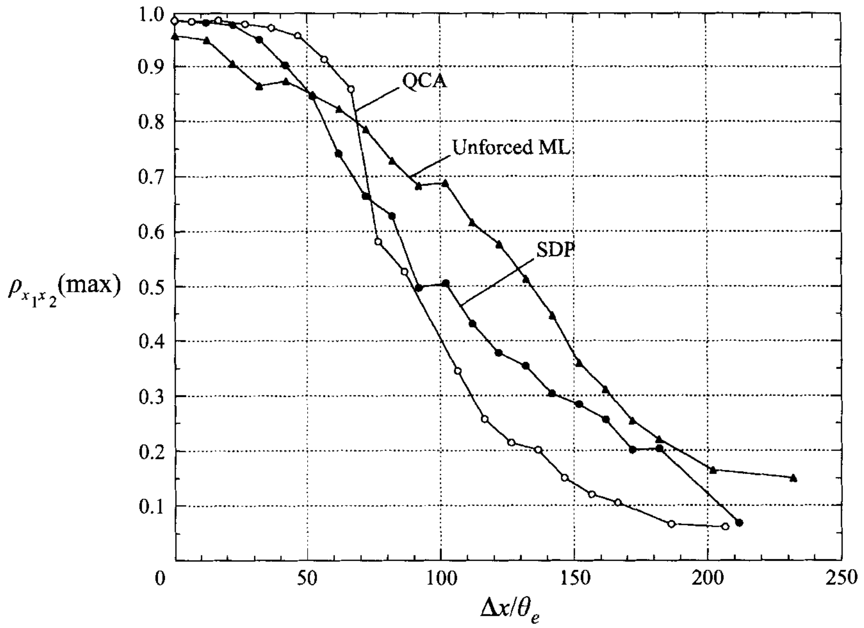

FIGURE 12. Spatial evolution of peak cross-correlation coefficient $\rho_{x_1x_2}$ for SDP, QCA and UML, for increasing probe separation $\Delta x/\theta_e$; the rapid decay implies loss of spatial correlation.

placement of probes (i.e. sampling locations) for developing spatiotemporal models from the data, and hence for devising intelligent open flow control strategies.

Studies to date of 'spatiotemporal dynamics' have been restricted to homogeneous spatially extended systems, in particular, closed flows such as large-aspect-ratio Rayleigh–Bénard convection (e.g. Heutmaker & Gollub 1987) and model systems of coupled map lattices (e.g. Kaneko 1984). Similar local events are spatially distributed in such flows. Correlation length ξ is typically used in these flows to quantify the spatial separation over which two signals become uncorrelated (see Hohenberg & Shraiman 1989). It is usually defined such that $R_{x_1x_2}(\Delta x) \sim \mathrm{e}^{-\Delta x/\xi}$, where $R_{x_1x_2}(\Delta x)$ is the peak of the two-point space–time correlation function $R_{x_1x_2}(\Delta x, \tau)$, and Δx (the separation) is non-dimensionalized by the appropriate lengthscale. When ξ becomes comparable to or less than the characteristic lengthscale (e.g. distance between horizontal plates in a large-aspect-ratio Rayleigh–Bénard experiment), local dynamics at the two locations become uncorrelated, and this flow state is termed spatiotemporal chaos (see Cross & Hohenberg (1993) for a review).

The spatial variation of dynamics (e.g. occurrence on different timescales) in spatially developing flows causes correlation to decay rapidly (i.e. small ξ), thereby indicating spatiotemporal dynamics; however, the dynamics at different locations may yet be coupled. Thus, the defining measure of coupling should be different in spatially developing flows. Measures general enough to describe spatiotemporal dynamics in any flow field are still lacking. We believe that coherence and cross-bicoherence are good indicators of coupling, and illustrate this in §§3.2 and 4.

3.1. *Cross-correlation*

A single-wire (reference) probe was positioned upstream of vortex roll-up ($30 \leqslant x/\theta_e \leqslant 40$), while a second probe was moved from roll-up to after the second pairing location ($30 \leqslant x/\theta_e \leqslant 250$); both probes were located at the high-speed edge of the ML, i.e. at the y-location where $U \approx 0.98\ U_e$. The cross-correlation coefficient (for zero-mean data) is

$$\rho_{x_1 x_2}(\tau) = \frac{R_{x_1 x_2}(\tau)}{\sigma_{x_1}\sigma_{x_2}}$$

where σ_{x_1} and σ_{x_2} are standard deviations of signals from the two probes, and the cross-correlation is

$$R_{x_1 x_2}(\tau) = \sum_{n=1}^{N-r} x_1(n)\, x_2(n+r) \quad (r = 0, 1, 2, \ldots, m),$$

where mh = maximum time delay, $rh = \tau$ (the time delay), and $h = 1/f_{sampling}$.

Cross-correlation measurements were made for SDP (at $St_{\theta_e} \approx 0.012$), QCA (at $St_{\theta_e} \approx 0.0165$) and UML for $90 \leqslant x/\theta_e \leqslant 300$ (see figure 12). Note that the maximum $\rho_{x_1 x_2} \neq 1$ as $\Delta x \rightarrow 0$, owing to slight inherent spanwise inhomogeneities (since $\Delta z \neq 0$; see figure 1). The rapid spatial decay of the peak $\rho_{x_1 x_2}(\tau)$, for all three cases, is due to the dominance of different frequencies in different flow regions, i.e. f, $\frac{1}{2}f$ and $\frac{1}{4}f$ near roll-up, first and second pairings, respectively. For SDP or QCA, first and second pairings always occur for $110 > \Delta x/\theta_e > 70$, thus providing very low correlation between a fundamental dominated (upstream) signal and a subharmonic/quarterharmonic dominated (downstream) signal. However, in an unforced flow, the aperiodic pairing is delayed in x (compared to SDP or QCA), thus providing relatively higher correlation farther downstream (see figure 12).

It is our expectation that the dynamics of periodic states are well coupled over a substantial spatial extent (including first and second pairing locations). However, we find the correlation length ξ to be in the range $50–80\theta_e$, for SDP and QCA; this is equivalent to at most two fundamental instability wavelengths (i.e. before completion of the first pairing). Thus, correlation measurements indicate that dynamics even in the domain that includes only the first pairing, let alone the periodic second pairing, is spatiotemporal.

3.2. *Coherence*

Since coupling implies the mutual dependence of dynamics at spatially separated points, we claim that the transfer function (between the two points) can provide an appropriate measure of coupling. Consider the simple case of system dynamics described by a linear transfer function, where coherence is the measure of linear coupling (see Appendix C for derivations and computation details) and is given by

$$\gamma^2(f) = \frac{|G_{x_1 x_2}|^2}{G_{x_1 x_1} G_{x_2 x_2}} = \frac{|\mathscr{F}[R_{x_1 x_2}(\Delta x, \tau)]|^2}{G_{x_1 x_1} G_{x_2 x_2}}$$

where $\mathscr{F}$ is the Fourier transform and G_{xx} is the spectral density function. Thus, when $\gamma^2(f) = 1$, the two points (x_1 and x_2) are perfectly linearly coupled. For the simplest case of a system which is dominated by a single frequency f (where $G_{xx}(f) = \sigma_x^2$), correlation loss is equivalent to coherence loss, and both reflect loss of coupling. But this equivalence does not hold for a spatially developing flow, where coherence at all dynamically significant frequencies may still remain high. We therefore believe that correlation measurement in such flows is not meaningful, but that coherence is an appropriate measure of coupling. Note that the presence of unmeasured sources (contributing to the downstream dynamics but not recorded in the upstream signal) could yield a decaying coherence and hence indicate an apparent loss of coupling; but, since the ML origin is the only conceivable point of receptivity in the flow, this possibility can be disregarded. For complicated dynamics governed by nonlinearities, higher-order transfer functions must be considered; we use cross-bicoherence as a measure of quadratic coupling in §4.

Coherence measurements were made in a forced jet by Bonetti & Boon (1989); coherence decay was related to the local chaotic attractor dimension and was claimed to indicate transition to turbulence. Coherence and bicoherence have also been used to infer transition to turbulence in a wake by Miksad, Jones & Powers (1983). We find that the decays of coherence and cross-bicoherence need not be associated with transition to turbulence, but merely indicate spatiotemporal dynamics.

We examined the evolution of peak coherence at dynamically significant frequencies resulting from forced roll-up and feedback-sustained periodic/modulated first and second pairings. The reference probe was positioned very close to the ML origin, at $x/\theta_e \approx 7$, while the second probe was traversed for $7 \leqslant x/\theta_e \leqslant 300$, i.e. beyond the second pairing location. Relative phases at the dominant frequencies were recorded at the high-speed edge (to reduce the uncertainty in phase measurements, which increases in the centre of the ML). For the phase measurements, the reference probe was positioned close to the roll-up location since the subharmonic phase there governs the modified growth rate (of the subharmonic) during subharmonic resonance (Monkewitz 1988; Husain & Hussain 1989).

3.2.1. *SDP*

Coherences at the fundamental, the subharmonic and the quarterharmonic remain high ($\geqslant 0.9$) for $x/\theta_e \leqslant 300$ (figure 13*a*). Such high coherences are accompanied by linear variations (with x) of the averaged relative subharmonic phase (appropriately unwrapped) shown in figure 13(*b*), indicating phase coherent signals; i.e. spatially coherent motion extends beyond the second pairing location ($x/\theta_e \approx 200$–220). However, phase velocities (inversely proportional to the slopes of the phase variation) of individual frequencies vary in different regions. The fundamental phase speed seems to remain constant up to completion of the second pairing ($x/\theta_e \approx 200$) with a slight variation after completion of the first pairing (presumably owing to generation of the fundamental as a harmonic of the subharmonic). The subharmonic maintains an almost constant phase speed (higher than that of the fundamental) up to completion of the first pairing ($x/\theta_e \approx 140$), while the quarterharmonic phase-velocity increases (above that of the subharmonic) for $x/\theta_e \geqslant 100$ and remains so up to $x/\theta_e \approx 130$ and for $x/\theta_e \geqslant 170$ (these trends are expected for subharmonic resonance from Monkewitz's (1988) theory). For $130 < x/\theta_e < 160$, the quarterharmonic phase speed fluctuation (increase and then decrease) indicates local phase jitter, i.e. slight aperiodicity during the second pairing (as speculated with regard to the $\frac{1}{4}f$ growth in §2.1.1). (Note that $\gamma^2(\frac{1}{4}f)$ variations, while remaining above 0.9, do not have any obvious correspondence with this phase-jitter.) Beyond $x/\theta_e = 300$, where the third pairing is completed, sharp coherence drops (not shown) suggest spatiotemporal dynamics. Coherence decay may also arise from nonlinear interactions; however, this is ruled out in §4 using cross-bicoherence measurements.

High-coherence at the fundamental is expected owing to its periodic forcing; however, the high coherences at the subharmonic and the quarterharmonic, implying strong coupling, can only be due to dominance of feedback. Thus, even though the flow is physically open, the dynamics are coupled over several instability wavelengths ($x/\lambda_f \approx 7$); i.e. the flow is spatially coupled and hence *dynamically closed.* (Note that $x/\lambda_f \approx 2St_{\theta_e}(x/\theta_e)$, where λ_f is the fundamental instability wavelength.)

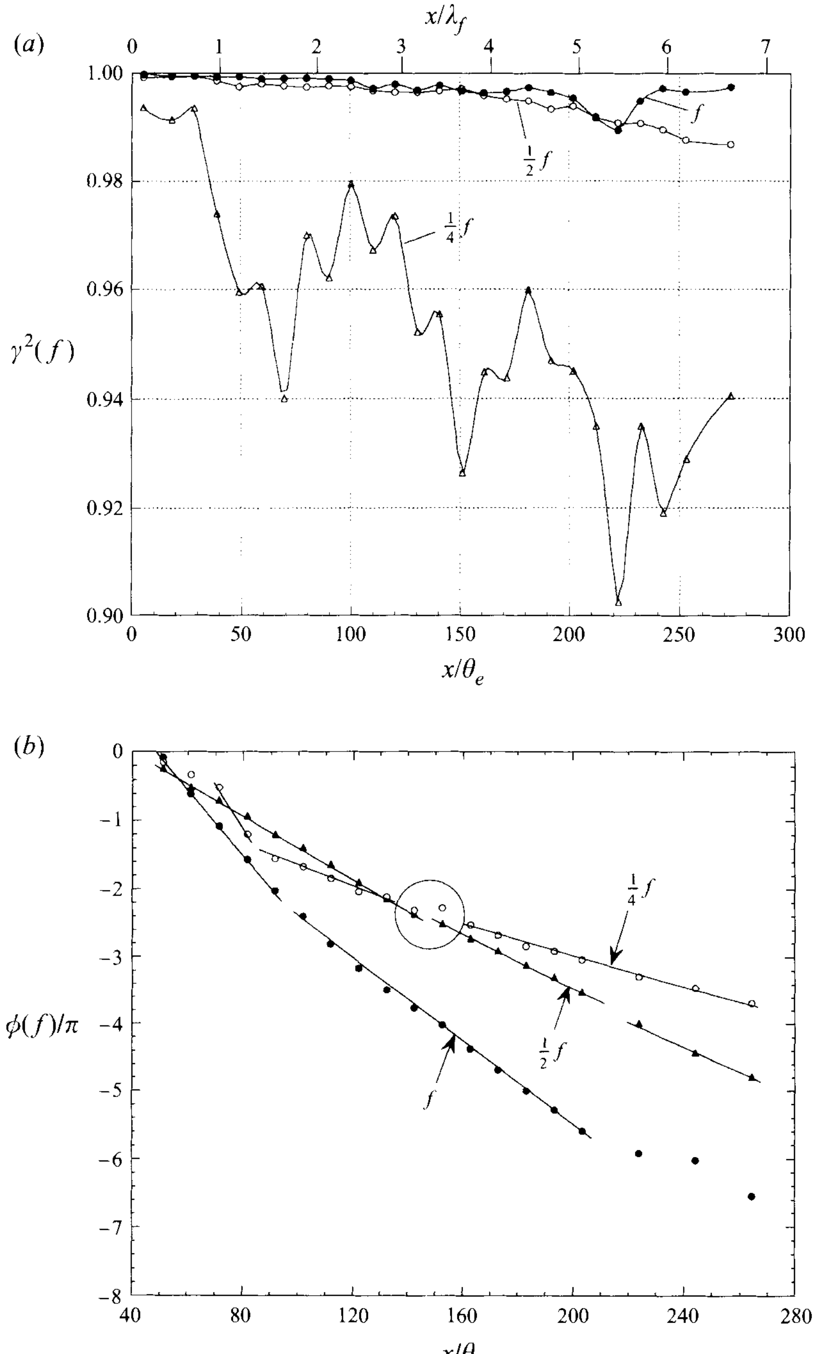

FIGURE 13. For SDP: (*a*) the evolution of peak coherence $\gamma^2(f)$ at the fundamental f, the subharmonic $\frac{1}{2}f$, and the quarterharmonic $\frac{1}{4}f$; and (*b*) the evolution of the relative phase $\phi(f)$ at the fundamental f, the subharmonic $\frac{1}{2}f$ and the quarterharmonic $\frac{1}{4}f$ with $\phi(\frac{1}{4}f)$ fluctuations for $130 < x/\theta_e < 160$ (the encircled area).

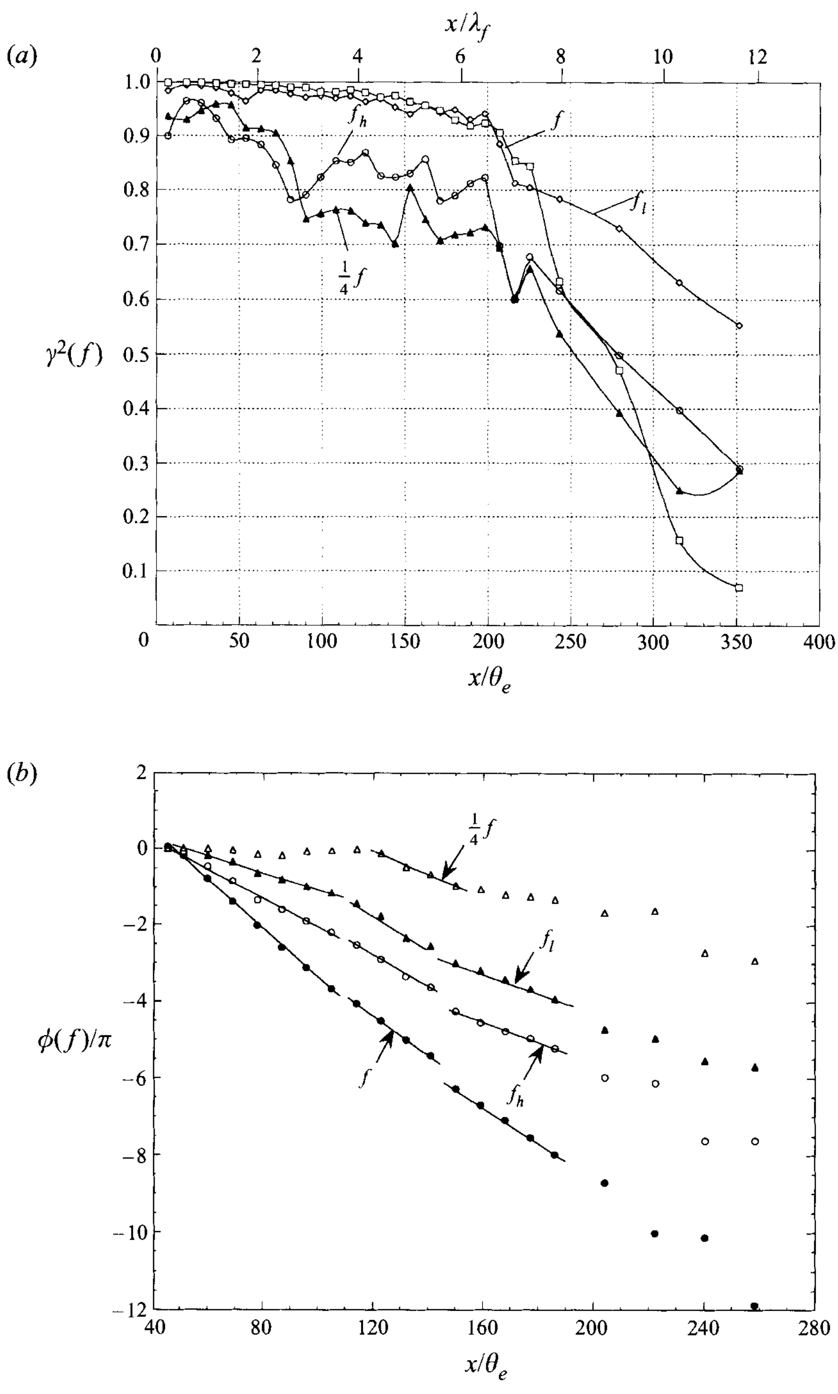

FIGURE 14. For QCA: (*a*) the peak coherence $\gamma^2(f)$ at the fundamental f, the sidebands (f_l, f_h) and the quarterharmonic $\frac{1}{4}f$ are high up to $x/\theta_e \approx 180$ and drop quickly at all frequencies thereafter; and (*b*) the evolution of the relative phase $\phi(f)$ at the fundamental f, the sidebands (f_l, f_h) and the quarterharmonic $\frac{1}{4}f$. Fluctuations of $\phi(f_l)$, $\phi(f_h)$ are prominent for $x/\theta_e > 180$, while linear dependence (with x) of $\phi(\frac{1}{4}f)$ is observed only during initial stages of the second resonance near $x/\theta_e = 110$.

3.2.2. *QCA*

Similar measurements for the chaotic attractor yielded peak coherences at the fundamental, the two sidebands and the quarterharmonic (peak of the broadband, see spectrum in figure 7*b*), shown in figure 14(*a*). Coherences at the fundamental f and the lower sideband f_l remain above 0.9 up to $x/\theta_e \approx 180$, while coherences at the higher sideband f_h and the quarterharmonic $\frac{1}{4}f$ show some decay following roll-up at $x/\theta_e \approx 70$ but remain above 0.7 up to $x/\theta_e \approx 180$, where chaotic second pairing occurs. The high coherences at all significant frequencies up to the second pairing location ($x/\lambda_f \approx 6$, $x/\theta_e \approx 180$–230) indicate spatial coupling. Beyond $x/\theta_e \approx 180$, the rapid decay of coherences at all these frequencies indicates progressive loss of coupling between the origin and the downstream locations, i.e. spatiotemporal dynamics. The relative phases at individual frequencies, shown in figure 14(*b*), support the claim of phase coherence (nearly linear variation of phase with x and high coherence values) at the sidebands up to $x/\theta_e \approx 160$. The fundamental phase velocity remains nearly constant up to the second pairing ($x/\theta_e \leqslant 180$) while the sidebands' phase speeds are unequal during the first pairing (i.e. for $x/\theta_e \leqslant 110$); the latter was also noted by Monkewitz (1988) for his 'detuned excitation' case (where sidebands were forced). The quarterharmonic phase does not vary significantly up to $x/\theta_e \approx 110$, after which its role in initiating the second resonance (i.e. the second pairing) becomes important, and its phase speed increases and remains constant for a short distance ($110 \leqslant x/\theta_e \leqslant 140$). For $x/\theta_e > 180$, the fluctuations in the phase are due to increased uncertainty in their measurements.

Highly coherent behaviour in the first pairing region indicates that although the instantaneous subharmonic phase at a fixed location varies, owing to shifting of the pairing location, its phase is well coupled to that at the origin (via advection of subharmonic perturbations and its feedback to the origin). The chaotic second pairing also provides feedback at aperiodic intervals causing the quarterharmonic phase at the origin (ϕ_q) to vary. However, in contrast to the first pairing, decaying coherence during second pairing reflects a quarterharmonic phase that is poorly matched with ϕ_q; i.e. the instantaneous phase difference varies from one pairing to the next. We speculate that the reason for this mismatch is the extreme sensitivity of chaotic dynamics to initial phase conditions. In addition, three-dimensionality in the evolution and interaction of vortices may cause this phase mismatch; this effect has not been investigated. We term the mismatch 'phase incoherence'.

3.2.3. *UML*

Figure 15 shows coherences at the fundamental (a broadband around $St_{\theta_e} \approx 0.01$) and the subharmonic (a broadband around $St_{\theta_e} \approx 0.0055$) for UML. The reference probe was positioned upstream of roll-up at $x/\theta_e \approx 65$ while the second probe was traversed between $65 \leqslant x/\theta_e \leqslant 300$. Coherences at the fundamental f and the subharmonic $\frac{1}{2}f$ remain above 0.9 up to $x/\theta_e \approx 120$, i.e. after completion of roll-up (saturation location of $St_{\theta_e} \approx 0.01$), but decay thereafter. It is surprising that the coherence at the aperiodic subharmonic remains at $\gamma^2(\frac{1}{2}f) \geqslant 0.7$ for $150 \leqslant x/\theta_e \leqslant 220$, indicating significant coupling in the region of aperiodic first pairing.

In §2 we found that low-level forcing of the UML triggers (spatially coupled) periodic pairing (especially for $St_{\theta_e} \approx 0.0115$ where the a_f required is the minimum among all St_{θ_e}); this is similar to the weak global mode that HM speculated in a uniform-density jet, which upon small forcing becomes unstable. Such behaviour of an unforced mixing layer (an open flow) is quite unexpected.

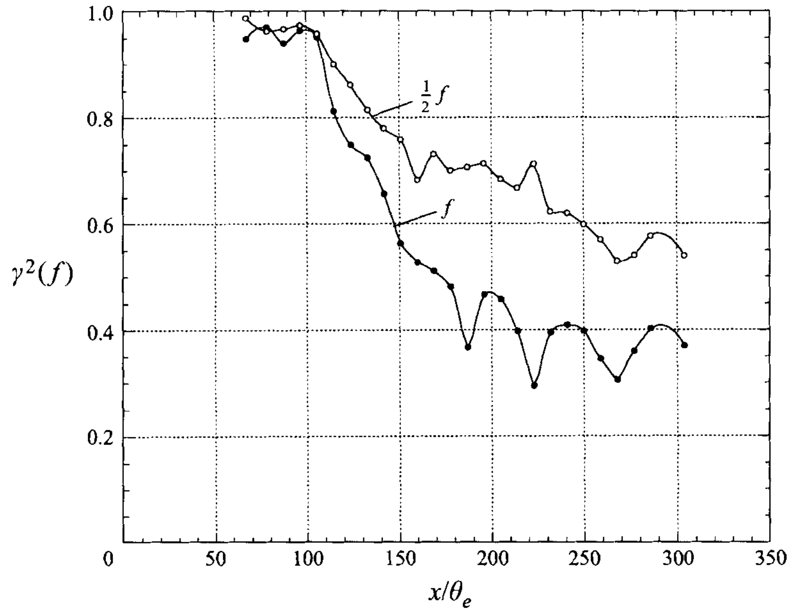

FIGURE 15. Evolution of peak coherence $\gamma^2(f)$ for UML at the broadband fundamental f and subharmonic $\frac{1}{2}f$. The $\gamma^2(f)$ decays rapidly following vortex roll-up but $\gamma^2(\frac{1}{2}f)$ remains relatively high during pairing ($160 \leqslant x/\theta_e \leqslant 230$) suggesting moderate coupling.

The results for SDP and QCA show that the dynamics at spatially separated points are coupled over a substantial domain, between the ML origin and the first/second pairing locations. This domain includes vortex roll-up and at least two vortex pairings for SDP but is restricted to roll-up and the first pairing for QCA. Single-point measurements made almost anywhere within these domains (and hence the low-dimensional attractors found in §2) adequately characterize the flow because of the spatial coupling. Downstream of the first pairing for QCA and the second pairing for SDP, coherence decay indicates loss of spatial coupling, i.e. spatiotemporal dynamics; this loss of spatial coupling is speculated to arise from chaotic feedback (see §3.2.2) and is investigated further in §§4 and 5. To study the advent of quadratic interactions during the first and second pairings, we have computed cross-bicoherence and discuss the results in the following section.

4. Role of nonlinear interactions

The ML dynamics beyond roll-up involve nonlinear growth and interactions of various instability frequencies (leading to vortex pairings). As indicated in §3, coherence decay may also arise from nonlinear effects, and when quadratic interactions occur in the flow, coherence alone is not a measure of coupling. The nonlinear generation of a particular frequency downstream from quadratic interactions of a pair of frequencies at an upstream location occurs from interactions (i) that are initiated between the two locations, and (ii) those initiated before the upstream location. Cross-bicoherence (see Appendix C for definition and computation details) captures quadratic interactions of the former type and is studied for SDP and QCA. A high cross-bicoherence ($\beta^2(f,f_1,f_2) \approx 1$) indicates strong quadratic coupling among the frequency triad (such that $f = f_1 + f_2$); i.e. it indicates how well f (at the downstream location) is phase coherent with f_1 and f_2 (at the upstream location). For these measurements the reference probe was positioned upstream of the fundamental saturation location (beginning of significant nonlinearity), while the second probe was traversed downstream of the second pairing location along the ray $U(y)/U_e \approx 0.98$.

4.1. *SDP*

Cross-bicoherences for the fundamental–subharmonic ($f-s$) interaction and the subharmonic–quarterharmonic ($s-q$) interaction were measured (figure 16) since these subharmonic resonances are the most significant quadratic interactions for SDP. Starting from the roll-up location, high $f-s$ cross-bicoherence indicates strong resonance, as expected for a stable first pairing. The $s-q$ cross-bicoherence levels are high ($\geqslant 0.9$) only beyond the first pairing location ($x/\theta_e \approx 110$), where the second pairing is initiated owing to the second resonance. The slight drop between $140 \leqslant x/\theta_e \leqslant 190$ corresponds to the region where the quarterharmonic growth is temporarily suppressed (see figure 3*c*); this supports our earlier speculation that the second pairing process is slightly aperiodic owing to local quarterharmonic phase jitter (see §3.2). Nevertheless, cross-bicoherence remains fairly high ($\geqslant 0.9$) up to $x/\theta_e \approx 350$, i.e. downstream of the second pairing.

The fact that both coherence (§3.2.1) and cross-bicoherence are high over a large region ($x/\theta_e \leqslant 300$, $x/\lambda_f \approx 7$), is evidence of spatial coupling in the SDP flow domain. We conclude that coherence decay, observed for $x/\theta_e \geqslant 300$ for SDP, is not simply a consequence of (quadratic) nonlinear interactions since even cross-bicoherence drops in this region. In fact, this decay of coherence and cross-bicoherence indicates spatiotemporal dynamics during the third pairing.

4.2. *QCA*

The interactions addressed here are those of the fundamental f and the higher sideband f_h producing the lower sideband $f_l(=f-f_h)$, and those of f and f_l producing $f_h(=f-f_l)$. The evolution of cross-bicoherences for these cases is displayed in figure 17. High levels of cross-bicoherence ($\geqslant 0.8$) for the $f-f_l$ and $f-f_h$ interactions are observed for $80 \leqslant x/\theta_e \leqslant 180$ (rapidly decaying farther downstream) indicating coupling up to the first pairing completion. Cross-bicoherence of the quarterharmonic $\frac{1}{4}f$ was found to be low ($\leqslant 0.1$) for interactions with any frequency chosen around the subharmonic, yet the second pairing occurs (as seen by modified $\frac{1}{4}f$ growth rate and its saturation in figure 7*c*). Thus $\frac{1}{4}f$ presumably undergoes nonlinear interactions (two-dimensional or even three-dimensional) with a range of frequencies around the subharmonic (hence providing a low, averaged cross-bicoherence for any particular triad). Beyond $x/\theta_e \approx 180$, where the second pairing occurs, no frequency triads could be identified which displayed substantial cross-bicoherence levels ($\geqslant 0.8$), showing that quadratic coupling is weak. Note that this coincides with the region where coherence decays at all significant frequencies. Thus, as concluded in §4.1, the coherence decay observed in §3.2.2 does not necessarily come from the onset of nonlinear phenomena (up to the second order). The low cross-bicoherence levels indicate phase mismatch (see §3.2.2) among the frequency triad (f, f_l, f_h). Higher-order nonlinear interactions (involving more than three frequencies) can produce low cross-bicoherence, but their physical significance is unclear.

From cross-bicoherence, we have found spatially coherent motion for the periodic and the chaotic attractors (involving two pairings in the case of SDP but only the first pairing for QCA). The region of decoupling (during the third pairing for SDP and during the second pairing for QCA) is inferred from decaying cross-bicoherence and

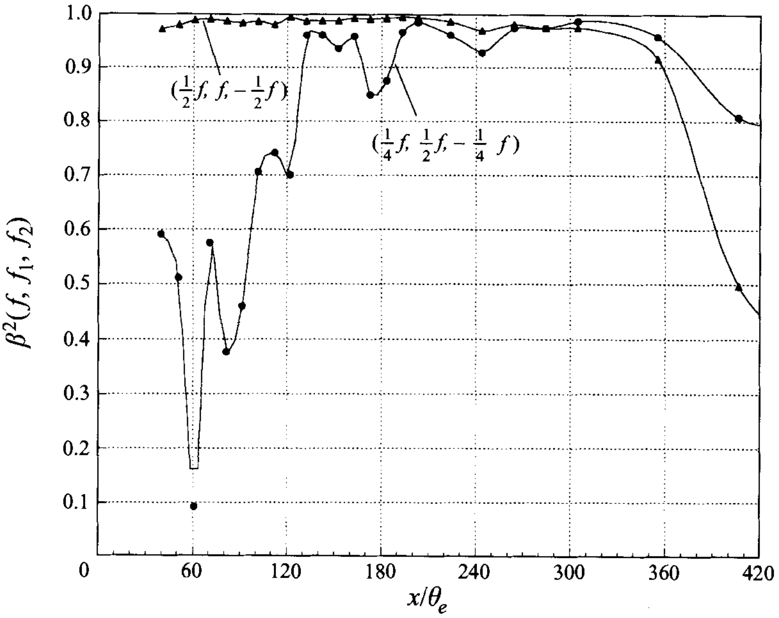

FIGURE 16. Spatial evolution of cross-bicoherence $\beta^2(f,f_1,f_2)$ for SDP involving quadratic interactions of the fundamental and the subharmonic, and the subharmonic and the quarterharmonic; $\beta^2(\frac{1}{4}f, \frac{1}{2}f, -\frac{1}{4}f)$ is high only for $x/\theta_e \geqslant 120$ where the second pairing is initiated and drops slightly for $130 \leqslant x/\theta_e \leqslant 190$ where quarterharmonic phase jitter is suspected.

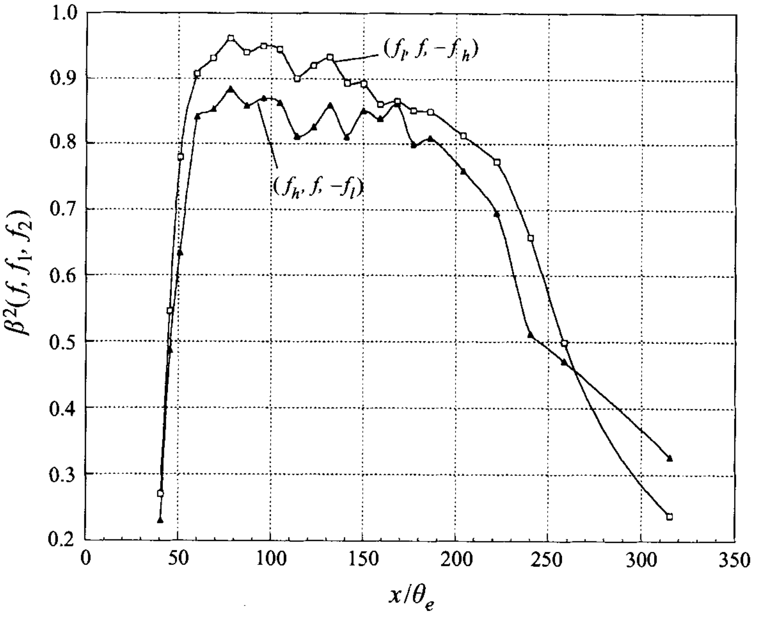

FIGURE 17. Spatial evolution of cross-bicoherence $\beta^2(f,f_1,f_2)$ for QCA involving quadratic interactions of the fundamental and sidebands; $\beta^2(f_h,f,-f_l)$ and $\beta^2(f_l,f,-f_h)$ are high only for $x/\theta_e \geqslant 80$ where the first pairing begins and sharply drop for $x/\theta_e \geqslant 180$ marking the onset of spatiotemporal dynamics.

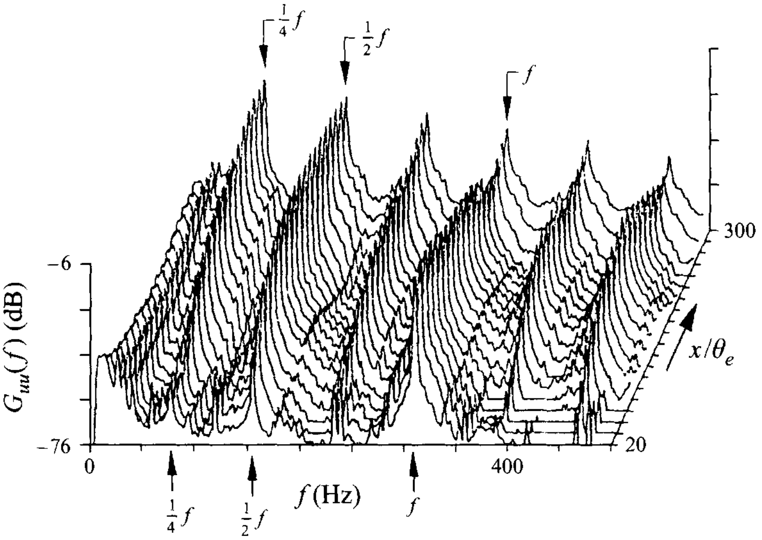

FIGURE 18. Power spectra at different x for SDP show periodicity, and growth followed by saturation of the fundamental, the subharmonic and the quarterharmonic; the last three spectra (at the largest x/θ_e values) were recorded with $\Delta x/\theta_e \approx 50$ while the others were recorded with $\Delta x/\theta_e \approx 10$.

is consistent with coherence fall-off observed in §3.2; this signifies spatiotemporal dynamics farther downstream involving phase incoherence (not to be confused with a transition to turbulence). During the second pairing for QCA, the chaotic dynamics cause small (undetectable) changes in the quarterharmonic phase at the origin to result in large variations farther downstream, thereby causing phase incoherence; this seems to be the mechanism for the loss of spatial coupling. We term this to be spatiotemporal chaos, wherein spatial and temporal disorder originate from deterministic chaos.

To summarize, high coherence and cross-bicoherence, at dynamically significant self-excited frequencies, over 'large' extents ($x \gg \lambda_f$) indicate spatial coupling in the flow. In the following, we analyse the effects of presence (or lack thereof) of spatial coupling on dynamical invariant measures used to describe the attractors in §2.

5. Spatial variations in temporal measures

To study the spatial development of the temporal attractors (SDP and QCA), spectra, correlation dimension ν, and the largest Lyapunov exponent λ were computed from signals sampled at different streamwise locations. Time traces and spectra were recorded at a few locations from upstream of roll-up to downstream of the second pairing location at intervals $\Delta x \approx 10\ \theta_e$. Estimates of ν and λ are reported only where ν has significant scaling regions (factor of at least 2), and both ν and λ converge quite well.

5.1. *SDP*

A spectral array for SDP ($St_{\theta_e} \approx 0.012$ and $a_f \approx 0.2\%$) is shown in figure 18, for $20 \leqslant x/\theta_e \leqslant 300$ along the $U(y)/U_e \approx 0.98$ line, displaying the dominance and periodicity of the fundamental, the subharmonic and the quarterharmonic frequencies close to roll-up, pairing and second pairing locations respectively.

The correlation dimension ν and the largest Lyapunov exponent λ are displayed as functions of the streamwise distance in figure 19(a,b). For most of the streamwise extent, $\nu \approx 1.1$–1.2 (m = 3) with $\lambda \approx 0$ b.p.o., indicating periodicity of roll-up, the first

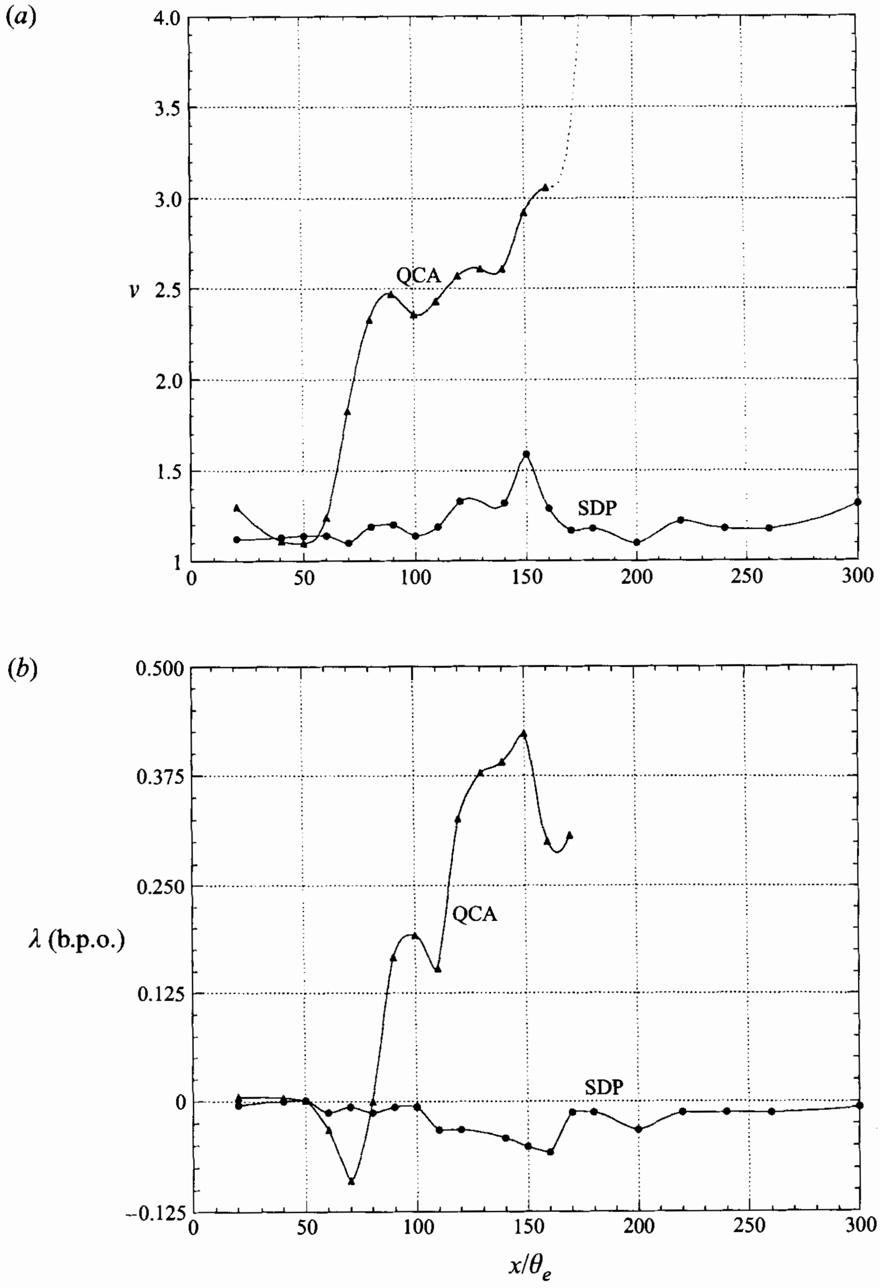

FIGURE 19. (*a*) Streamwise variation of correlation dimension ν for a periodic (SDP) and a chaotic (QCA) attractor. The almost constant ν $(=2.3\text{–}2.6)$ for QCA in the region $90 \leqslant x/\theta_e \leqslant 160$ corresponds to chaotic features of the attractor, and the slight increase of ν (>1.2) for SDP around $x/\theta_e = 150$ reflects phase jitter during initial stages of the second pairing. The dashed line for QCA represents speculated increase of ν based upon dimension calculations which yielded small scaling regions and poor convergence. (*b*) Streamwise variation of the largest Lyapunov exponent (λ, b.p.o.) for SDP and QCA; $\lambda > 0$, indicating chaos, is observed for QCA where $2.3 \leqslant \nu \leqslant 2.6$.

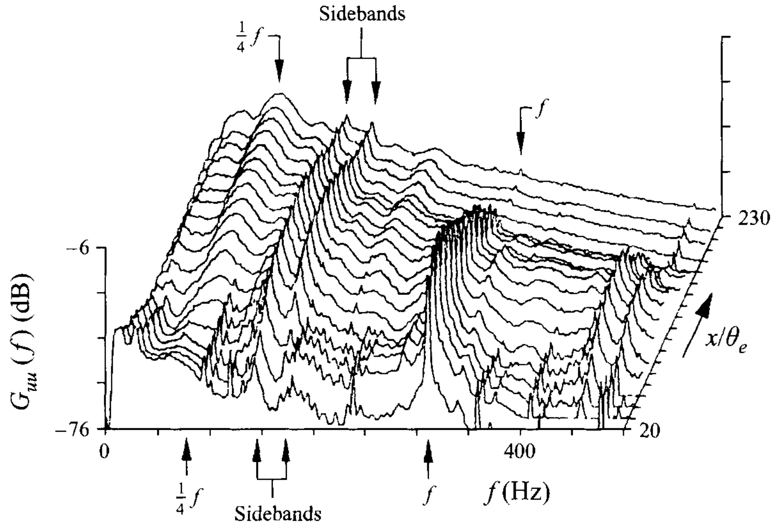

FIGURE 20. QCA power spectra at different x shows sequential growth and saturation of the fundamental, the sidebands and the broadband quarterharmonic; the last three spectra are recorded with $\Delta x/\theta_e \approx 25$ while the others were recorded with $\Delta x/\theta_e \approx 10$.

and the second pairings. We find that ν is high (1.3–1.6) and λ is negative ($-0.064 \leqslant \lambda \leqslant -0.032$ b.p.o.) in a region between the first and the second pairing locations (around $x/\theta_e = 150$). Based upon discussions in §2.1.2 (for SP) we infer that such ν and λ estimates indicate noisy limit cycles. The slight aperiodicity during second pairing may be due to jitter in pairing, or three-dimensionality. Quarterharmonic growth suppression and small fluctuations in our phase and cross-bicoherence measurements over this region suggest quarterharmonic phase jitter (see §2.1.1). This jitter is reduced once the second pairing is complete; consequently, farther downstream, ν and λ indicate periodic dynamics.

The fact that features of a periodic attractor are captured almost everywhere over $4 \leqslant x/\theta_e \leqslant 300$ is evidence of the spatial extent of order in the flow and is consistent with the results in §§3.2 and 4.

5.2. *QCA*

Spectra for $St_{\theta_e} \approx 0.017$, $a_f \approx 0.2\,\%$ in the region $20 \leqslant x/\theta_e \leqslant 230$ are shown in figure 20. The initial dominance of the fundamental, the growth and saturation (by $x \approx 90\ \theta_e$) of the two sidebands around the subharmonic (remaining distinct up to $x \approx 130\ \theta_e$) and emergence of a broadband quarterharmonic (near $x = 100\ \theta_e$) are consistent with the growth patterns discussed in §2.1.3. For $x \geqslant 130\ \theta_e$, the spectral background increases and is dominated by the broadband quarterharmonic; this increased spectral broadening is a consequence of phase incoherence (inferred from coherence and cross-bicoherence decay), not necessarily indicative of transition to turbulence.

Correlation dimension for QCA at different x is shown in figure 19(*a*). For $x/\theta_e \leqslant 60$, $\nu \approx 1.1$–1.3 ($m = 4$) and $\lambda \approx 0$ b.p.o., owing to periodic roll-up. However, for $60 < x/\theta_e \leqslant 90$, ν increases to 1.82, while λ is sizeably negative ($-0.089 \leqslant \lambda \leqslant -0.032$ b.p.o., see figure 19*b*). The probe in this region senses the effects of periodic roll-up and modulated pairing, thus dimension calculations yield an averaged ν estimate ($1 < \nu < 2$). Farther downstream, where chaotic modulations of the second pairing are sensed, chaotic dynamics ($\nu \approx 2.2$–2.5 and $\lambda \approx 0.128$–0.449 b.p.o.) are found over a sizeable flow region ($90 \leqslant x/\theta_e \leqslant 150$). For

$x/\theta_e > 160$, dimension estimates quickly exceed 3, scaling regions for ν diminish and convergence is poor. This sudden increase in dimension corresponds to the onset of spatiotemporal dynamics (inferred from decaying coherence and cross-bicoherence in §3.2.2 and §4.2).

We have thus verified the spatial extent over which the dynamical system is essentially temporal (having periodic or chaotic dynamics). There are some locations (around $x/\theta_e = 150$ for SDP, and $x/\theta_e \leqslant 90$ for QCA) where single-point measurements yield inconclusive results (e.g. $1 < \nu < 2$) and reflect only local dynamics (e.g. $\nu \approx 1$ for $x/\theta_e \leqslant 60$ in QCA). A sudden increase in ν for $x/\theta_e > 160$ is associated with the loss of spatial coupling (inferred in §§3 and 4).

6. Concluding remarks

The extreme sensitivity of convectively unstable (open) flows to external disturbances makes downstream flow prediction seemingly impossible using single-point measurements. However, in the presence of spatial coupling, even such complex open flow dynamics are tractable. We recommend the following approach to describe open flow dynamics: (i) use standard dynamical systems techniques to identify low-dimensional states (if any), and then (ii) identify dynamically significant phenomena (such as vortex pairings in jets and mixing layers, bursting and streaky structures in boundary layers (Jeong & Hussain 1992)) and associated frequencies, and compute coherence and cross-bicoherence to measure coupling. Step (i) describes transitional dynamics in terms of low-dimensional attractors, and step (ii) discerns the temporal (spatially coupled) or spatiotemporal (uncoupled) nature of the attractors in appropriate flow regions.

In the presence of spatial coupling, the transitional forced mixing layer is found to behave as a temporal dynamical system over several instability wavelengths. Spatially separated points are dynamically coupled via advecting rolled up and pairing vortices and feedback to the flow origin (receptivity point); evidence of feedback from pairings is provided. The spatially coupled dynamics is confined to periodic and low-dimensional chaotic attractors found in a wide region of the control parameter space. The finding of low-dimensional attractors opens up prospects for intelligent, nonlinear control of open shear flows using novel techniques such as chaos control (Ott, Grebogi & Yorke 1990). A forced axisymmetric jet (BH) and the forced mixing layer are found to have similar spectra, dimensions and largest Lyapunov exponents for the periodic (SDP) and chaotic (QCA) states. This is not too surprising because of the similar evolutionary vortex dynamics (i.e. roll-up and feedback-sustained pairings) in both flows.

Measurements of coherence and cross-bicoherence were used to determine the spatial extent of the temporal dynamical system summarized above; high coherence at significant frequencies for the periodic and even chaotic attractors are additional evidence of strong feedback. The periodic attractor SDP is found to be spatially coupled well beyond the second pairing location. For the chaotic attractor QCA, dynamics up to the first pairing is seen to be spatially coupled. Farther downstream, during the chaotic second pairing, decaying coherence and cross-bicoherence indicate loss of coupling which is accompanied by a large increase in the dimension. In the absence of spatial coupling it is impossible to predict the dynamics at any point in the flow from knowledge about the dynamics only at another location. We speculate that, for the chaotic attractor, the spatial disorder (loss of coupling) observed farther downstream is caused by temporal chaos (see §4.2), and hence term the resulting downstream dynamics *spatiotemporal chaos*. However, a quantitative characterization of this behaviour is lacking since analyses of other possible mechanisms for spatiotemporal chaos (such as three-dimensionality and transition to turbulence) require multiprobe measurements; unfortunately, no obvious experimental approach for this is evident.

A quantitative description of spatiotemporal dynamics (currently lacking) might require devising new measures (derived from signals sampled simultaneously in space and time), which may provide sophisticated models for prediction and control of open shear flows. The use of coherences suggested here seems to be ideal for choosing optimal sensor number, placement and spacing for the modelling. The development of multipoint techniques, if possible, may yield dimension and Lyapunov exponents for spatiotemporal systems. An added concern in developing such tools is to ensure that the invariant measures are intensive, i.e. do not depend on the domain size, especially in a spatially developing flow (where increasing the domain size could change dimension estimates since different modes dominate in different flow regions). Dimension density is one such measure which is based upon estimation of a two-point dimension (Pomeau 1985), but is restricted to homogeneous flows (Mayer-Kress & Kurz 1987). Also, transfer function estimation provides a means to predict the dynamics at another spatial location from measurements at a single location; i.e. it is an ideal measure of the predictability. These studies are beyond the scope of the present paper, and some are being pursued. Nevertheless, our combined approach (using dynamical systems and two-point spectral measures) can be used to describe coherent structure dynamics in a wider class of open shear flows, such as boundary layers, jets and wakes.

We are grateful to Drs George Broze and Davinder Virk for reviews of the manuscript. This work, excerpted from the MS thesis of SN, was supported by the Office of Naval Research grant N00014-89-J-1361 and the Air Force Office of Scientific Research grant F49620-95-1-0302.

Appendix A. Description and qualification of experimental facility

The newly built plane mixing layer facility (schematic shown in figure 21*a*) is attached to a 15.25 cm diameter, 77 m long iron pipe connecting the blower to the circular pipe (*P*) entering the anechoic chamber (shown schematically in figure 21*b*). The chamber is an air-conditioned concrete box (0.3 m thick walls) set on 44 air bearings with 1 m long fibreglass wedges lining the entire inner wall surface so that the chamber dimensions are 7.5 m × 5 m × 5 m from wedgetip to wedgetip. The interior ambient sound level is 35 dB above 100 Hz. Vertical pipes attached to the bottom of the chamber provide traverse support. The configuration of the facility prior to entering the chamber is documented in Bridges (1990). The flow loop, having only large radius bends to minimize secondary flow, has a cooling coil outside the anechoic chamber to control the supply air temperature which otherwise increases with blower velocity. A filter removes 95% of dust particles above the size of 2 μm. The blower requires some settling time ($\approx$ 1–2 hours) to stabilize the temperature and blower oscillations.

Individual facility sections

The extended facility (inside the anechoic chamber) comprises a circular-to-square (CS) section, a diffuser, a settling chamber and a nozzle. Air enters the chamber

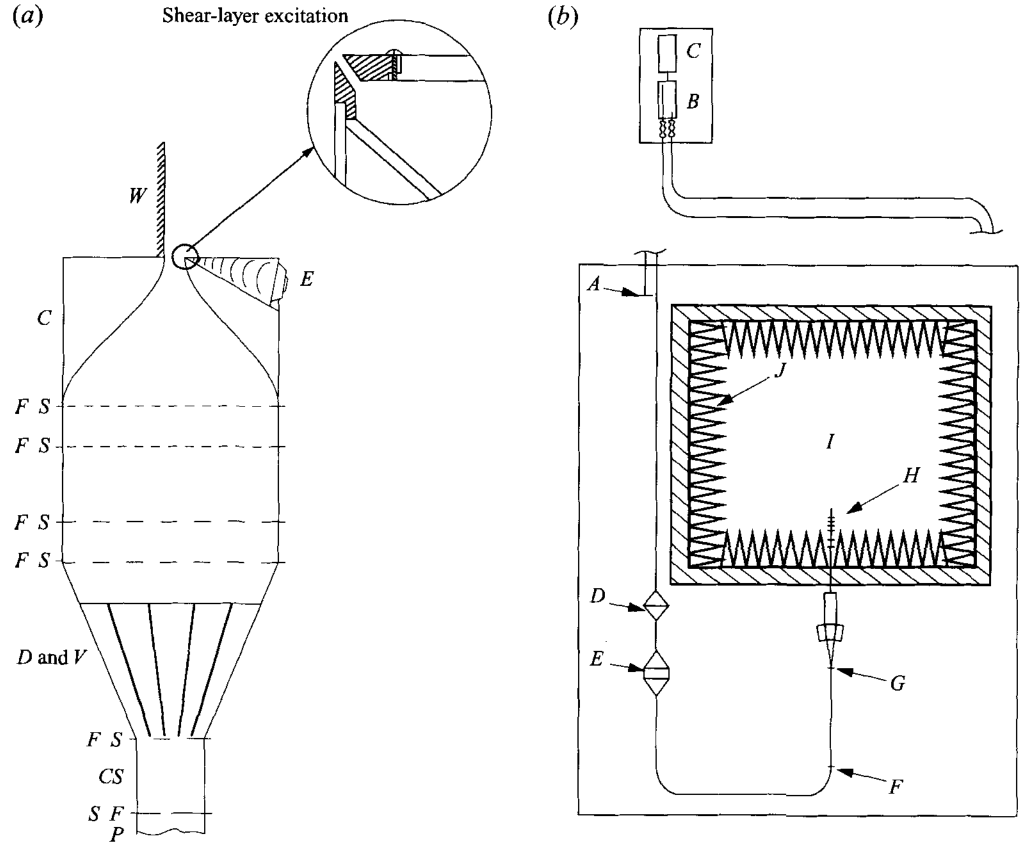

FIGURE 21. (*a*) Schematic of the plane mixing-layer facility, showing the settling chamber with the flow conditioners used; the exit excitation chamber is also illustrated. ———, 18 mesh; ——, 24 mesh; ---, 30 mesh. *P*, pipe; *CS*, circular-to-square section; *D*, diffuser; *V*, vanes; *S*, screen; *F*, flange; *C*, contraction; *E*, excitation; *W*, wall. (*b*) Schematic showing facility attachments prior to the mixing-layer facility and the anechoic chamber where experiments were conducted. *A*, air intake; *B*, compressor with muffler and vibration isolating couplings; *C*, DC motor; *D*, electrostatic filter; *E*, heat exchanger; *F*, screen; *G*, honeycomb; *H*, plane mixing-layer facility; *I*, anechoic chamber; *J*, fibreglass wedges.

through a 91.4 cm long, 15.24 cm diameter pipe, to which the 30.48 cm long CS section with an inlet diameter of 15.24 cm and a 17.78 cm × 17.78 cm square exit is attached (figure 21*a*). A 24-mesh screen at the entry of this section ensures uniform flow at the pipe exit ($\bar{U}/U_c > 98\,\%$ for more than 95 % of the entire cross-section), and also serves to trip the flow at the walls causing the flow to remain attached to all the walls. We have ensured that $Re_d < 40$ (d is the screen wire diameter) so that there is no vortex shedding from the screen wires. Open areas for all screens exceed 57 % to prevent non-uniform flow downstream of the screen (Bradshaw 1964). The CS is followed by a square diffuser (*D* in figure 21*a*) with a 17.78 cm × 17.78 cm inlet and a 50 cm × 50 cm exit (an area expansion of 7.91), providing a 14.8° half-angle expansion over a distance of 60.96 cm. To totally suppress separation, a set of four, 0.229 cm thick, aluminium splitter vanes were installed in the diffuser, producing a half-angle of approximately 2.8° in each cell. Termination of the vanes at about 60 % of the length of the section was found to be sufficient for flow conditioning. The vane spacing was set to account for the momentum deficit in the growing boundary layers on the diffuser walls, thereby

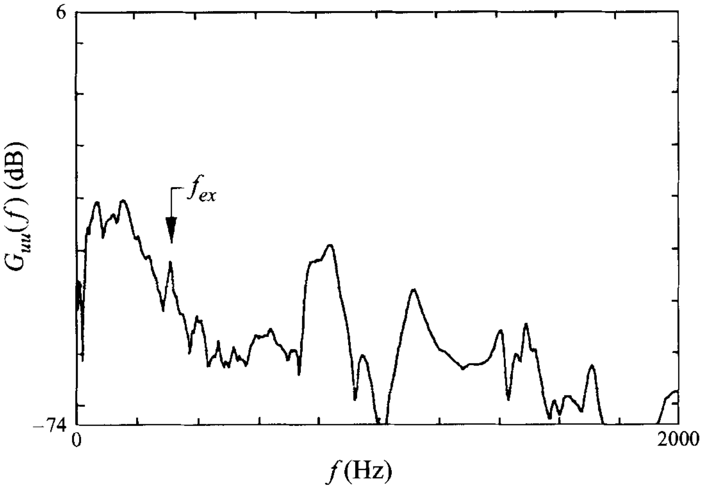

FIGURE 22. Transfer function of the excitation chamber shows frequencies supported by the chamber. The excitation frequency chosen for the present experiments is indicated as f_{ex}.

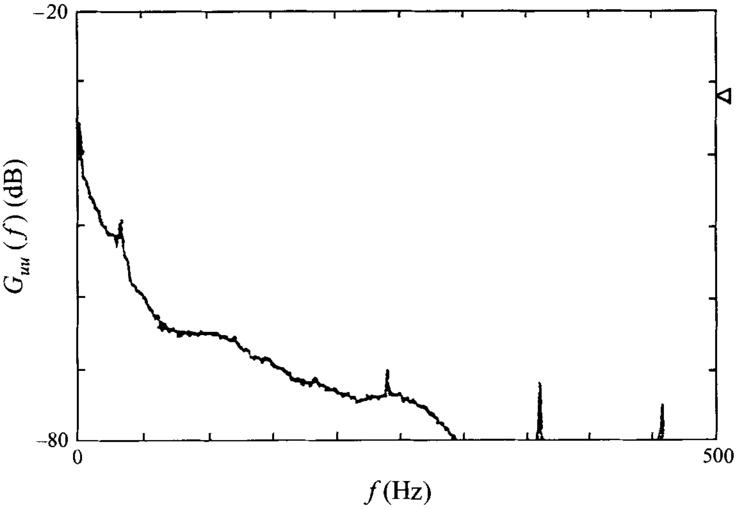

FIGURE 23. Exit boundary-layer spectrum. Note that the lack of discrete frequencies (besides the small peak around 28 Hz) indicates a minimally disturbed boundary layer.

ensuring a uniform flow at the exit. Sharp knife-edges of the vanes at the inlet and the exit minimize vane wakes.

A 53.34 cm long settling chamber with flow conditioning screens follows the diffuser. Two 24-mesh screens (66 % open area) were placed at the diffuser exit and 600 d after the diffuser (a spacing of 500 d is recommended for fine mesh screens by Laws & Livesey 1978). Two 30-mesh screens (61.4 % open area) follow the second 24-mesh screen at about 1200 d and then 600 d farther downstream. The flow after each screen was measured to ensure progressively more uniform mean velocity profiles and decreasing turbulence intensity levels. The exit mean velocity of the settling chamber is uniform (to within ±2 % of centreline velocity) across more than 98 % of the cross-section. An overshoot of velocity ($\approx$ 2–3 %) is detected close to the walls.

A 7.62 cm long straight section follows the fourth screen to the nozzle contraction. The two-dimensional contraction has a cubic polynomial profile with a contraction

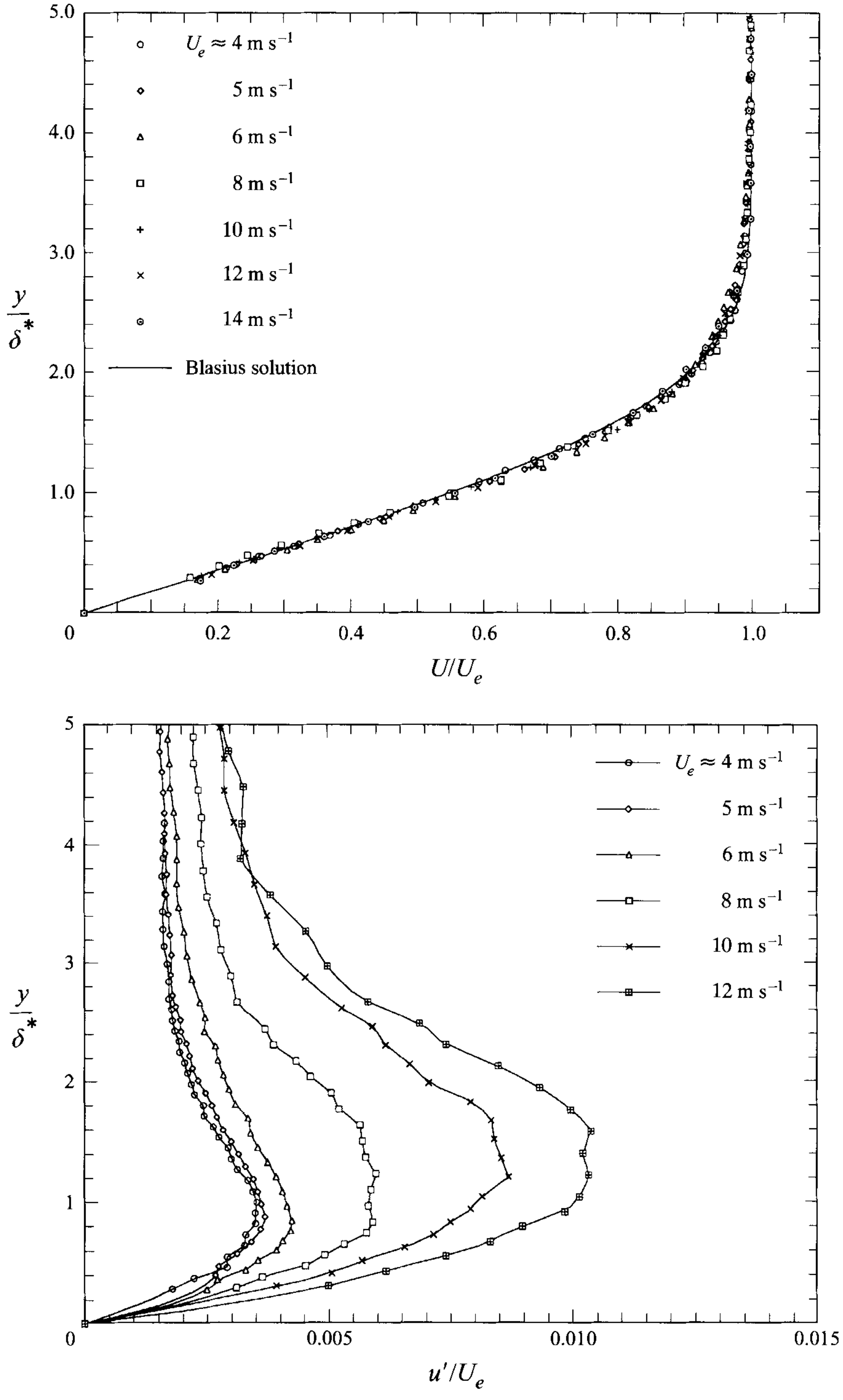

FIGURE 24. (*a*) Mean velocity profile in the exit boundary layer; it agrees well with the Blasius solution for a laminar boundary layer; (*b*) r.m.s.-velocity fluctuation profile in the exit boundary layer with $u'_{max}/U_e \leqslant 1\,\%$ (indicative of a 'nominally' laminar boundary layer).

ratio of 10:1, an exit aspect ratio of 10:1 (length $L = 50$ cm, slit width $w = 5$ cm), and a 38.1 cm wall extending on one side; the anechoic chamber wedges are at least 10000 θ_e downstream of the nozzle exit. A 2.5 cm ($= \frac{1}{2}w$) straight section is provided at the entry of the nozzle, and a similar 1.25 cm section at the exit. The straight section at the entry and the 7.62 cm straight section before the nozzle provide a 600 d long section before the contraction. A shear-layer excitation system (three 4″, 10 W woofer speakers) has been installed close to the shear-layer lip (see inset in figure 21*a*). Sharp-edged aluminium blocks have been used at the exit to enable adjustment and to ensure a uniform excitation slit width ($\leqslant 1$ mm). The excitation chamber transfer function shows the discrete frequencies at which the chamber supports excitation (figure 22). The excitation frequency was chosen to be 312 Hz to achieve the desired St_{θ_e} range (0.006–0.024) with $U_e \leqslant 12$ m s^{-1} (for which the exit boundary layer is laminar). The transfer function of the settling chamber and the contraction was also inspected, and no abnormal resonances were detected.

Exit characteristics

The mean velocity ($\bar{U}$) profiles at the nozzle exit (without the wall) obtained at several spanwise locations are uniform ($< 2.5\%$ variation in $\bar{U}$). A $\bar{U}$ profile measured by a Pitot tube did not indicate any overshoot, suggesting that the overshoot (≈ 2–3%) detected by the hot-wire may be due to flow cooling close to walls. The exit centreline longitudinal turbulence intensity was less than 0.1% for $U_e \leqslant 12$ m s^{-1}.

The exit boundary layer characteristics indicate 'nominally laminar' boundary layers (Hussain 1983) for velocities up to 12 m s^{-1}, i.e. a shape factor in the range 2.5–2.65, low peak turbulence intensity ($u'_{max}/U_e \leqslant 1\%$), and no discrete frequencies in the spectrum recorded in the boundary layer (see figure 23) except a small peak at 28 Hz (which is presumably a room acoustic mode). The mean and r.m.s.-fluctuation velocity profiles are shown in figure 24(*a*, *b*); a high-pass filter (5 Hz) was used followed by amplification of the fluctuations to improve the accuracy in calculating the r.m.s.-velocity fluctuation. A transitional boundary layer was detected at 16 m s^{-1}, wherein peak fluctuation levels increased ($\geqslant 2\%$) and the shape factor reduced to 2.24. The boundary-layer exit r.m.s.-velocity profiles are uniform in the spanwise direction; i.e. they vary from the profile at the centreline (in z) by less than $\pm 6.5\%$.

Transition to turbulence?

To detect transition to small-scale turbulence, the slope of the velocity spectrum in the inertial subrange was examined at various streamwise ($180 \leqslant x/\theta_e \leqslant 900$) and transverse locations ($0.4 \leqslant U/U_f \leqslant 1$, where U_f is the freestream velocity). Using a $-\frac{5}{3}$ slope as an indicator of turbulence, we find that transition occurs between 300 and 500 θ_e from the exit, i.e. after second-pairing. For SDP, transition is evidenced only after completion of a third pairing.

Shear layer–boundary layer interactions

In order to ensure that the ML grows independently of the boundary layer (BL) on the (opposite) wall, any possible coupling of shear layer and BL must be examined. By maintaining a high w/θ_e ratio (> 170 here) we expect to minimize this interaction. The interaction was analysed via two-point measurements conducted simultaneously on the wall and the ML side.

Using a special boundary-layer probe on the boundary-layer side and a long-prong probe on the ML side, conditional averaging (using at least 1024 realizations) was performed on a spectrum analyzer using the ML probe signal for the trigger; both

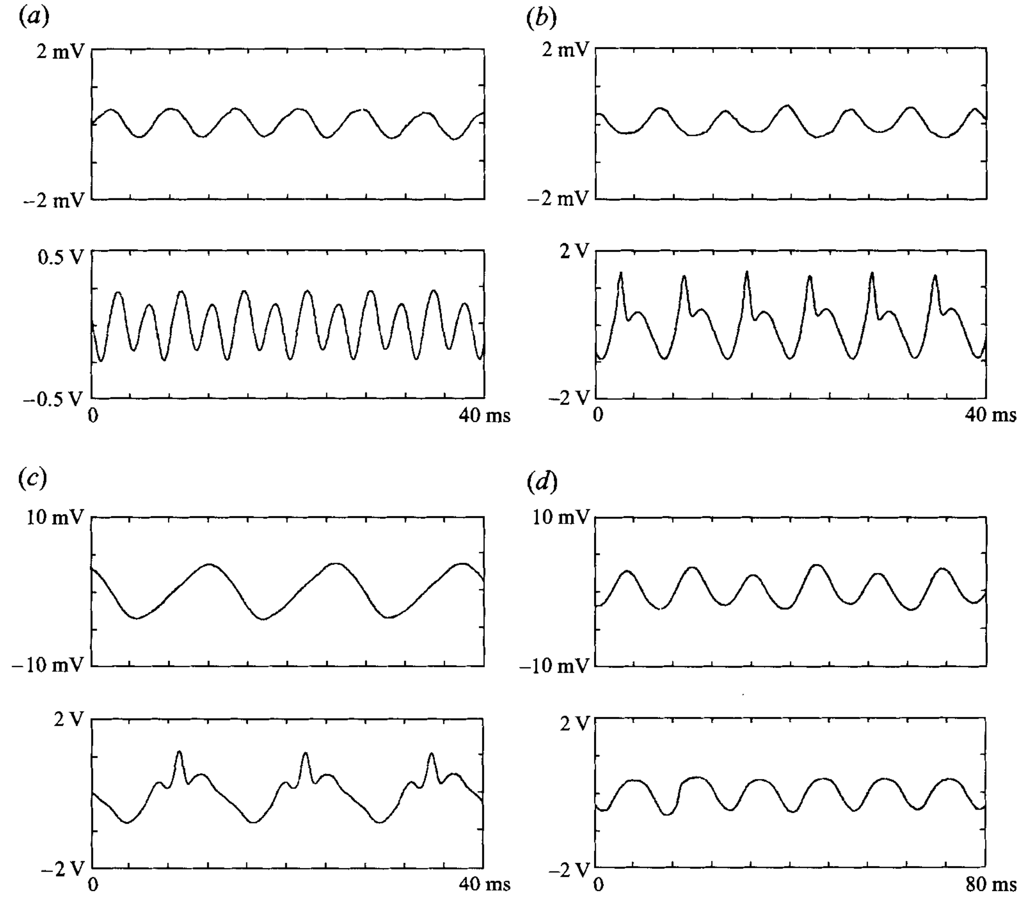

FIGURE 25. Time traces of the longitudinal velocity from the two shear zones across the potential core, the boundary layer (top) and the shear layer (bottom) side, at: (*a*) $x/\theta_e \approx 50$, (*b*) 100, (*c*) 200, (*d*) 500; the transverse location in each case is chosen such that the peak-to-peak voltage variation is maximum. The peak-to-peak voltages in the top time traces are 2–3 orders of magnitude below those in the lower traces showing that the shear layer-boundary layer interaction in the facility is weak.

probes were calibrated for the same velocity and voltage ranges. This exercise was performed for SDP, with $St_{\theta_e} \approx 0.012$ and $a_f \approx 0.2\%$, at various streamwise locations ranging from $50 \leqslant x/\theta_e \leqslant 500$. Suitable periodic triggers were chosen at different streamwise locations, e.g. based on f at $x/\theta_e \approx 50$ (roll-up location) and $\frac{1}{2}f$ at $x/\theta_e \approx 100$ (prior to first pairing). Transverse locations of both probes were chosen such that maximum fluctuations at significant frequencies (f, $\frac{1}{2}f$, $\frac{1}{4}f$) were obtained. Results of this experiment are shown in figure 25(*a*–*d*); in each figure the top signal is from the BL while the bottom one is from the ML. As is evident from the time traces, the fundamental, the subharmonic and the quarterharmonic survive the average on the BL side close to roll-up, first and second pairing locations, respectively. However, the peak-to-peak voltage difference on the BL side is always at least 2 orders of magnitude less than that on the ML side. The r.m.s.-velocity fluctuation profiles for f, $\frac{1}{2}f$ and $\frac{1}{4}f$ were measured at various streamwise locations ($x/\theta_e \approx 100$, 200 and 500) across the flow; large differences, one or two orders of magnitude, in u'_{max}/U_e inside the BL and the SL, indicate weak coupling (up to $x/\theta_e \approx 500$). The flow can thus be regarded as a 'nominally free' shear layer over the streamwise extent of our experiments.

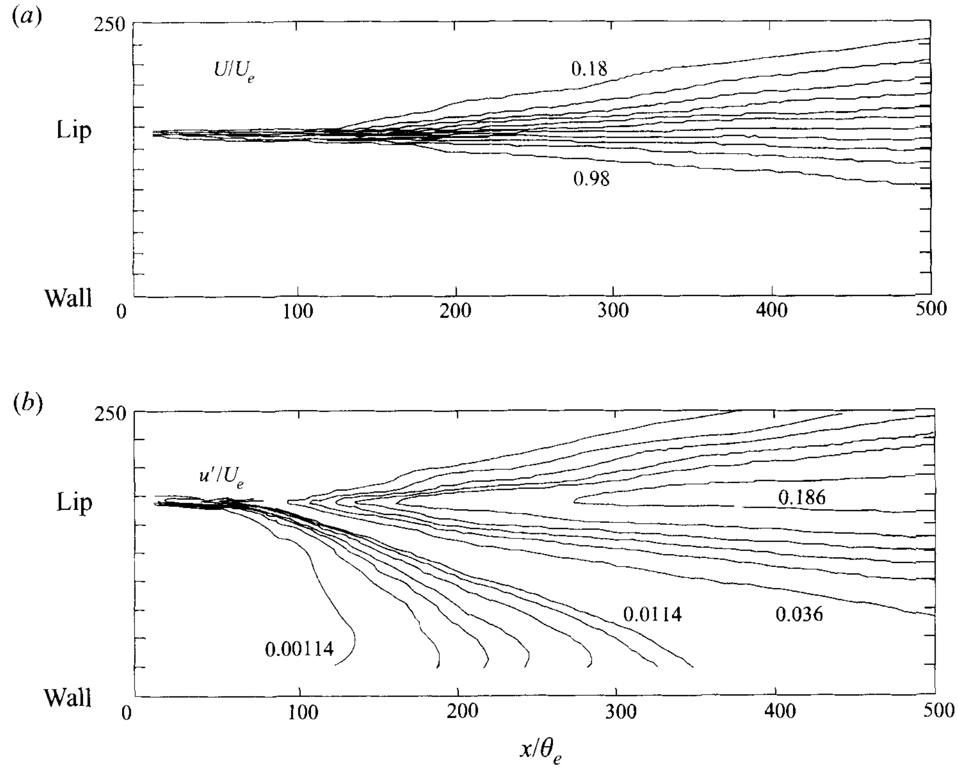

FIGURE 26. (*a*) Normalized mean velocity (U/U_e) distribution in the unforced ML; the minimum and maximum contour levels are 0.18 and 0.98, respectively, with an interval of 0.08. (*b*) Normalized r.m.s.-velocity (u'/U_e) distribution in the unforced ML; for $0.00114 \leqslant u'/U_e \leqslant 0.0114$ the contour interval is 0.0025, and for $0.036 \leqslant u'/U_e \leqslant 0.186$ the interval is 0.03.

Exit slit width of the contraction (w)	5 cm
Contraction ratio in the nozzle	10:1
Exit aspect ratio	10:1
Exit velocity range (Re_w range)	2–16 m s^{-1} (6.7×10^3–5.3×10^4)
Exit momentum thickness range (θ_e)	0.1441–0.4846 mm
Exit Re_{θ_e} range	64–154
Critical lengthscale parameter (w/θ_e)	> 170 (for $U_e > 5$ m s^{-1})
Natural roll-up frequency (St_{θ_e})	0.01–0.013

TABLE 1. Summary of important facility characteristics

Instantaneously, vortices in an unforced ML may agglomerate to create structures large enough (in circulation) to sweep fluid from the BL and alter the ML dynamics. Since no unique type of structure exists in the flow, the choice of a periodic trigger (as for SDP) is not possible. However, instantaneous time traces (observed simultaneously on the ML and BL sides) do not show any appreciable large-scale (correlated) motion; instantaneous peak-to-peak magnitude of the BL fluctuations is at least two orders of magnitude lower than that on the ML side. The time average velocity field of the unexcited ML (see figure 26) shows the ML spread; the 98 % U/U_e velocity line is used as an indicator of the location beyond which the potential region starts and extends until one reaches the BL. As can be seen from the time-averaged ML spread, up to

$x/\theta_e \approx 500$ the 98% velocity line remains more than 100 θ_e from the wall. Also $(u'_{max}/U_e)_{wall\text{-}side} \approx 1.2\%$, which is an order of magnitude lower than that on the ML side. These results indicate that even for the unexcited ML there may not be significant interactions between the shear layer and the BL structures. Table 1 summarizes some important facility characteristics.

Computer and data acquisition system

All the data were acquired on a Masscomp MC6650 computer using a real-time UNIX operating system. Time series were acquired using a 12 bit A/D converter with simultaneous sample-and-hold boards capable of acquiring data at 1 MHz. Data acquired from the hot wire were low-pass filtered at 5 kHz (using Krohn-Hite 3341 analog filters) before sampling. Fluctuation amplitudes of individual spectral components were recorded on a two-channel Ono Sokki 920 spectrum analyser (after high-pass filtering at 10 Hz) with a 16 bit A/D converter. Dimension and Lyapunov exponent calculations were performed on the Cray Y-MP at the NASA Ames Research Center.

Probes, traverse and excitation system

A 4 μm diameter and 2 mm long tungsten–rhodium hot wire (single-wire boundary-layer probe TSI-1218), and two single wires with 25 mm (TSI-1210 CS) and 5 mm long prongs, with a 1.4 overheat ratio, were employed for all measurements. An x–y traverse system with stepper motor control (Slo-Syn SS-150-1021 and SS-400-1010 with 0.025 mm resolution) was used for probe movement. A 2 MHz function generator (Wavetek model 20) and a Hafler model P500 stereo power amplifier were used for excitation.

Appendix B. Dynamical systems techniques employed

In addition to time traces and their discrete Fourier transforms, DS measures were used to analyse temporal dynamics. Sufficiently long time series (typically 100000 data points) sampled at 40 times the dominant frequency (f, $\frac{1}{2}f$ or $\frac{1}{4}f$) were used for computing the following measures and to provide well-resolved Poincaré sections.

(i) Mutual information (MI): MI for discrete signals is given by

$$I(S,Q) = \sum_{ij} P_{sq}(s_i,q_j)\log\left\{\frac{P_{sq}(s_i,q_j)}{P_s(s_i)\,P_q(q_j)}\right\}$$

where P_{sq}, P_s, P_q are the probability density functions (PDF) of the two signals. MI quantifies the time connectivity, i.e. correlation, between two time traces (they could be two different time series or time-delayed versions of the same sample). We have used sample sizes larger than 50000 points with 32 bins for MI computations. Details of evaluating the PDFs and errors involved in the computations are discussed in Broze (1992).

(ii) Correlation dimension (ν): This provides a measure of the attractor geometry. The attractor, reconstructed in time-delay coordinates, is displayed in a phase portrait, i.e. the graph $[u(t), u(t+\tau)]$. For a self-similar object, power law scaling, $C(r) \sim r^\nu$, is expected, and

$$C(r) = \lim_{N\to\infty} \frac{1}{N^2} \sum_{i,j=1}^{N} \theta(r - |X_i - X_j|),$$

where θ is the Heaviside function and r is the radius of a sphere in an m-dimensional phase-space (Grassberger & Procaccia 1983). Details of ν computation, its validation, and the choice of the minimum embedding dimension (note that $C(r)$ is evaluated for several m) for extracting ν are documented in Broze (1992).

(iii) Largest Lyapunov exponent (λ): The exponent quantifies the rate of exponential convergence/divergence of trajectories in phase space. A necessary and sufficient condition for a system to be chaotic is at least one positive Lyapunov exponent. The exponent is given by,

$$\lambda = \lim_{t \to \infty} \frac{1}{t} \ln \frac{d(t)}{d(0)}$$

where d is the distance between two neighbouring trajectories in phase-space. The algorithm developed by Wolf *et al.* (1985) was used to estimate the largest λ (in b.p.o.). This λ computation requires *a priori* specification of the range of phase-space scales (r_{min} and r_{max} for $C(r)$ discussed above); r_{min} and r_{max} define the range for which ν 'scales' (i.e. is virtually unchanged with r). Calculation of λ was performed separately for each such range found (as in §2.1.2).

Surrogate data analyses

This method provides a means to detect intrinsic nonlinear dynamics in a stationary time series (Theiler *et al.* 1992). The approach is to specify a well-defined underlying linear stochastic process (called the null hypothesis), then generate a surrogate data set from this process, which is examined for the quantity of interest, e.g. correlation dimension. If this quantity is different from that for the original process then the null hypothesis is rejected and the original process is declared to be nonlinear. The surrogate data set is generated from the original data set as follows: the Fourier transform $X(f)$ of the original data is computed from a large window of the data set (at least 2^{16} points) to avoid leakage effects from using a rectangular window. The transform is then decomposed into an amplitude $A(f)$, and a phase $\phi(f)$, i.e. $X(f) = A(f) \exp(i\phi(f))$. A set of phases $\phi_s(f)$ on the interval $[-\pi, \pi]$ is generated using a uniform distribution random number generator and substituted for $\phi(f)$, thus producing a surrogate Fourier transform $X_s(f) = A(f) \exp(i\phi_s(f))$. Now, the inverse Fourier transform of $X_s(f)$ is computed to yield $x_s(t)$, the surrogate data set.

Appendix C. Spectral measures: coherence and cross-bicoherence

We use coherence $\gamma^2(f)$ and cross-bicoherence $\beta^2(f, f_1, f_2)$ to identify linear and quadratic coupling among a set of frequencies. These measures were used in the studies of turbulence in plasmas and for detecting quadratic interactions in transitional shear flows (Miksad *et al.* 1983). The representation of a nonlinear transfer function was provided by Ritz & Powers (1986), and we have used relevant expressions to extract coherences, and justify our usage of coherence and cross-bicoherence as measures of coupling. The analyses were carried out with a simplified model for the system transfer function that is restricted to linear and quadratic interactions.

$$X(f) \longrightarrow \boxed{H(f)} \longrightarrow Y(f)$$

In general, $Y(f) = H(f)\, X(f)$, which is expanded as,

$$Y(f) = L(f)\, X(f) + \sum_{f_1 f_2} Q^{f_1 f_2}(f)\, X(f_1)\, X(f_2) + \epsilon(f), \tag{C 1}$$

where $L(f)$ denotes the linear transfer function, $Q^{f_1 f_2}(f)$ denotes the quadratic transfer function accounting for interactions among a triad of frequencies (such that $f_1 + f_2 = f$), and $\epsilon(f)$ includes estimation errors (from averaging) and contribution from all higher-order interactions. The summation is over frequencies such that $f_1 \geqslant f_2$. Note that, the fourth-order moment $\langle X(f_1)\,X(f_2)\,X^*(f_1')\,X^*(f_2')\rangle$ is approximated by $\langle|X(f_1)\,X(f_2)|^2\rangle$ and $Q^{f_1f_2}(f)\,Q^{f_1'f_2'*}(f) \approx |Q^{f_1f_2}(f)|^2$ (after averaging over sufficiently large number of ensembles), where, * denotes complex conjugate, and $f_1'+f_2'=f_1+f_2=f$. Such an approximation implies that frequencies such that $f_1 \neq f_1'$ and $f_2 \neq f_2'$ are neglected in the averaging process. To verify this approximation we performed a few tests (using 50 ensembles) and found that the magnitude of the fourth-order moment from considering (f_1',f_2') terms are less than 5% of that from considering (f_1,f_2) terms; moreover, the cumulative contribution to the fourth-order moment from all pairs of (f_1',f_2') is also less than 10% of that from considering (f_1,f_2) alone. Multiplying (C 1) by its complex conjugate, ensemble averaging and dividing throughout by $\langle|Y(f)|^2\rangle$ gives,

$$1 = \underset{\text{(term I)}}{|L(f)|^2\frac{\langle|X(f)|^2\rangle}{\langle|Y(f)|^2\rangle}} + \underset{\text{(term II)}}{\sum_{f_1f_2}|Q^{f_1f_2}(f)|^2\frac{|\langle X(f_1)\,X(f_2)\rangle|^2}{\langle|X(f)|^2\rangle\langle|Y(f)|^2\rangle}}$$

$$+\underset{\text{(term III)}}{2Re\left[L(f)\sum_{f_1f_2}Q^{f_1f_2^*}(f)\frac{\langle X(f)\,X^*(f_1)\,X^*(f_2)\rangle}{\langle|Y(f)|^2\rangle}\right]}+\underset{\text{(term IV)}}{\frac{\langle|\epsilon(f)|^2\rangle}{\langle|Y(f)|^2\rangle}}. \tag{C 2}$$

These represent the linear (I, denoted as $\gamma_L^2(f)$), quadratic (II, denoted as $\gamma_Q^2(f)$) and linear-quadratic coupling (III, denoted as $\gamma_{LQ}^2(f)$) terms, and errors (term IV); $L(f)$ and $Q^{f_1f_2}(f)$ are assumed to be uncorrelated with $\epsilon(f)$. $L(f)$ and $Q^{f_1f_2}(f)$ can be derived from (C 1) to be (see Ritz & Powers 1986),

$$L(f) = [\langle Y(f)\,X^*(f)\rangle - \sum_{f_1f_2}Q^{f_1f_2}(f)\,\langle X^*(f)\,X(f_1)\,X(f_2)\rangle - \langle\epsilon(f)\,X^*(f)\rangle]/\langle|X(f)|^2\rangle \tag{C 3}$$

$$Q^{f_1f_2}(f) = \frac{\langle Y(f)\,X^*(f_1)\,X^*(f_2)\rangle - L(f)\,\langle X(f)\,X^*(f_1)\,X^*(f_2)\rangle - \langle\epsilon(f)\,X^*(f_1)\,X^*(f_2)\rangle}{\langle|X(f_1)\,X(f_2)|^2\rangle} \tag{C 4}$$

Substituting (C 3) and (C 4) in (C 2) and neglecting cross-terms involving $\langle|\epsilon(f)|^2\rangle$ provides the following estimates for $\gamma_L^2(f)$ and $\gamma_Q^2(f)$,

$$\gamma_L^2(f) \approx \gamma^2(f) + \sum_{f_1f_2}|Q^{f_1f_2}(f)|^2\frac{|\langle X^*(f)\,X(f_1)\,X(f_2)\rangle|^2}{\langle|X(f)|^2\rangle\langle Y(f)|^2\rangle}$$

$$-2\frac{\langle Y(f)\,X^*(f)\rangle}{\langle|X(f)|^2\rangle\langle|Y(f)|^2\rangle}\sum_{f_1f_2}Q^{f_1f_2}(f)\,\langle X^*(f)\,X(f_1)\,X(f_2)\rangle$$

where $\gamma^2(f) = |\langle Y(f)\,X^*(f)\rangle|^2/\langle|X(f)\;{}^2\rangle\langle|Y(f)|^2\rangle$ (used as *coherence* in the present study).

$$\gamma_Q^2(f) \approx \sum_{f_1f_2}\beta^2(f,f_1,f_2) + |L(f)|^2\sum_{f_1f_2}\frac{|\langle X^*(f)\,X(f_1)\,X(f_2)\rangle|^2}{\langle|X(f_1)\,X(f_2)|^2\rangle\langle|Y(f)|^2\rangle}$$

$$-2L(f)\sum_{f_1f_2}\frac{\langle Y(f)\,X^*(f_1)\,X^*(f_2)\rangle\,\langle X^*(f)\,X(f_1)\,X(f_2)\rangle}{\langle|X(f_1)\,X(f_2)|^2\rangle\langle|Y(f)|^2\rangle}$$

where $\beta^2(f,f_1,f_2) = |\langle Y(f)\,X^*(f_1)\,X^*(f_2)\rangle|^2/\langle|X(f_1)\,X(f_2)|^2\rangle\langle|Y(f)|^2\rangle$ (used as *cross-bicoherence* in this study).

Note that $|\langle X^*(f)\,X(f_1)\,X(f_2)\rangle|^2/\langle|X(f_1)\,X(f_2)|^2\rangle\,\langle|X(f)|^2\rangle$ (termed *auto-bicoherence*) represents quadratic coupling at the input itself. In the absence of such coherent triads at the input, i.e. $|\langle X^*(f)\,X(f_1)\,X(f_2)\rangle| = 0$, $\gamma_L^2(f)$ and $\gamma_Q^2(f)$ reduce exactly (to within estimation errors) to the expressions for coherence and cross-bicoherence, while $\gamma_{LQ}^2(f) = 0$.

Significance of coherence and cross-bicoherence

A high coherence at $f(\gamma^2(f) \approx 1)$ indicates linearity at f (i.e. no phase distortion) between the two signals. There are three possible implications of $\gamma^2(f) < 1$ (Bendat & Piersol 1986): (i) measurement noise in the first or the second signal, (ii) an additional input, unaccounted for at the first signal, or (iii) system nonlinearity. Cross-bicoherence $\beta^2(f,f_1,f_2)$ represents the degree of quadratic coupling for a triad of frequencies, such that $f_1 + f_2 = f$. A $\beta^2(f,f_1,f_2) < 1$ indicates weak quadratic interactions in between the two signals implying linearity or higher-order nonlinear interactions. Computation of $\gamma_L^2(f)$ and $\gamma_Q^2(f)$ involves estimation of auto-bicoherence (found to be non-zero in our experiments) and a computationally intensive iterative procedure to extract $L(f)$ and $Q^{f_1 f_2}(f)$ (Ritz & Powers 1986). However, to detect linear/quadratic coupling in the flow, this much detail is unnecessary; thus, we estimated only $\gamma^2(f)$ and $\beta^2(f,f_1,f_2)$.

All spectral quantities, such as autospectra, cross-spectra, and their derivatives, such as coherence and cross-bicoherence, were computed on the Masscomp computer using averages over at least 80–100 records. Each record, sampled at 2048 Hz, was 2048 points long.

REFERENCES

BENDAT, J. S. & PIERSOL, A. G. 1986 *Random Data Analysis and Measurement Procedures*, 2nd edn. Wiley-Interscience.

BONETTI, M. & BOON, J.-P. 1989 Chaotic dynamics in an open flow: the excited jet. *Phys. Rev.* A **40**, 3322.

BRADSHAW, P. 1964 Wind tunnel screens: flow instability and its effect on aerofoil boundary layers. *J.R. Aeronaut. Soc.* **68**, 198.

BRANDSTÄTER, A., SWIFT, J., SWINNEY, H. L., WOLF, A., FARMER, J. D. & JEN, E. 1983 Low-dimensional chaos in a hydrodynamic system. *Phys. Rev. Lett.* **51**, 1442.

BRIDGES, J. E. 1990 Application of coherent structure and vortex sound theories to jet noise. PhD dissertation, University of Houston.

BROWN, G. B. 1937 The vortex motion causing edge tones. *Proc. Phys. Soc.* **49**, 493.

BROZE, G. 1992 Chaos in an 'open' flow: experiments in transitional jets. PhD dissertation, University of Houston.

BROZE, G. & HUSSAIN, F. 1994 Nonlinear dynamics of forced transitional jets: periodic and chaotic attractors. *J. Fluid Mech.* **263**, 93 (referred to herein as BH).

BROZE, G. & HUSSAIN, F. 1996 Transition to chaos in a forced jet: intermittency, tangent bifurcations and hysteresis. *J. Fluid Mech.* **311**, 37.

CROSS, M. C. & HOHENBERG, P. C. 1993 Pattern formation outside of equilibrium. *Rev. Mod. Phys.* **65**, 851.

DEISSLER, R. J. & KANEKO, K. 1987 Velocity-dependent Lyapunov exponents as a measure of chaos for open-flow systems. *Phys. Lett.* **119**, 397.

DIMOTAKIS, P. E. & BROWN, G. L. 1976 The mixing layer at high Reynolds number: large-structure dynamics and entrainment. *J. Fluid Mech.* **78**, 535.

DUBOIS, M. 1982 Experimental aspects of the transition to turbulence in Rayleigh–Bénard convection. *Stability of Thermodynamic Systems*. Lecture Notes in Physics, vol. 164, p. 117.

FRASER, A. & SWINNEY, H. L. 1986 Independent coordinates for strange attractors from mutual information. *Phys. Rev.* A **33**, 1134.

FREYMUTH, P. 1966 On transition in a separated laminar boundary layer. *J. Fluid Mech.* **25**, 683.

GRASSBERGER, P. & PROCACCIA, I. 1983 Measuring the strangeness of strange attractors. *Physica* D **9**, 189.

GRINSTEIN, F. F., ORAN, E. S. & BORIS, J. P. 1991 Pressure field, feedback, and global instabilities of subsonic spatially developing mixing layers. *Phys. Fluids* A **3**, 2401.

HEUTMAKER, M. S. & GOLLUB, J. P. 1987 Wave-vector field of convective flow patterns. *Phys. Rev.* A **35**, 242.

HO, C.-M. & HUERRE, P. 1984 Perturbed free shear layers. *Ann. Rev. Fluid Mech.* **16**, 365.

HOHENBERG, P. C. & SHRAIMAN, B. I. 1989 Chaotic behavior of an extended system. *Physica* D **37**, 109.

HUERRE, P. 1987 Spatio-temporal instabilities in closed and open flows. In *Instabilities and Nonequilibrium Structures* (ed. E. Tirapegui & D. Villaroel), p. 141. Reidel.

HUERRE, P. & MONKEWITZ, P. A. 1990 Local and global instabilities in spatially developing flows. *Ann. Rev. Fluid Mech.* **22**, 473 (herein referred to as HM).

HUSAIN, H. S. & HUSSAIN, F. 1989 Subharmonic resonance in a shear layer. In *Advances in Turbulence 2* (ed. H. H. Fernholz & H. E. Fiedler), p. 96, Springer; see also *J. Fluid Mech.* **304**, 343 (1995).

HUSSAIN, F. 1983 Coherent structures – reality and myth. *Phys. Fluids* **26**, 2816.

HUSSAIN, F., HUSAIN, H. S., ZAMAN, K. B. M. Q., TSO, J., HAYAKAWA, M., TAKAKI, R. & HASAN, M. A. Z. 1986 Free shear flows: organized structures and effects of excitation. *AIAA paper* 86–0235.

HUSSAIN, F. & ZAMAN, K. B. M. Q. 1978 The free shear layer tone phenomenon and probe interference. *J. Fluid Mech.* **87**, 349.

JEONG, J. & HUSSAIN, F. 1992 Coherent structure near the wall in a turbulent boundary layer. *The Fifth Asian Congress of Fluid Mechanics, Aug. 10–14, Taejon, Korea*, vol. 21, p. 1262.

KANEKO, K. 1984 Period-doubling of kink-antikink patterns, quasiperiodicity in antiferro-like structures and spatial intermittency in coupled logistic lattice. *Prog. Theor. Phys.* **72**, 202.

KELLY, R. E. 1967 On the stability of an inviscid shear layer which is periodic in space and time. *J. Fluid Mech.* **27**, 657.

LAWS, E. M. & LIVESEY, J. L. 1978 Flow through screens. *Ann. Rev. Fluid Mech.* **10**, 247.

MATHIS, C., PROVANSAL, M. & BOYER, L. 1984 The Bénard–von Kármán instability: an experimental study near the threshold. *J. Phys. Lett. Paris* **45**, L483.

MAYER-KRESS, G. & KURZ, T. 1987 Dimension densities for turbulent systems with spatially decaying correlation functions. *Complex Systems* **1**, 821.

MICHALKE, A. 1965 On spatially growing disturbances in an inviscid shear layer. *J. Fluid Mech.* **23**, 521.

MIKSAD, R. W., JONES, F. L. & POWERS, E. J. 1983 Measurements of nonlinear interactions during natural transition of a symmetric wake. *Phys. Fluids* **26**, 402.

MONKEWITZ, P. A. 1988 Subharmonic resonance, pairing and shredding in the mixing layer. *J. Fluid Mech.* **188**, 223.

MONKEWITZ, P. A., BECHERT, D. W., BARSIKOW, B. & LEHMANN, B. 1990 Self-excited oscillations and mixing in a heated round jet. *J. Fluid Mech.* **213**, 611.

MONKEWITZ, P. A., HUERRE, P. & CHOMAZ, J. M. 1993 Global linear stability of weakly non-parallel shear flows. *J. Fluid Mech.* **251**, 1.

OSTER, D. & WYGNANSKI, I. 1982 The forced mixing layer between parallel streams. *J. Fluid Mech.* **123**, 91.

OTT, E., GREBOGI, C. & YORKE, J. A. 1990 Controlling chaos. *Phys. Rev. Lett.* **64**, 1196.

POMEAU, Y. 1985 Méchanique des fluides – measure de la densité d'information en turbulence. *C.R. Acad. Sci. Paris*, **300**, Série II(7), 239.

RASMUSSEN, D. R. & BOHR, T. 1987 Temporal chaos and spatial disorder. *Phys. Lett.* A **125**, 107.

REISENTHEL, P. 1988 Hybrid instability in an axisymmetric jet with enhanced feedback. PhD dissertation, Illinois Institute of Technology.

RITZ, CH.P. & POWERS, E. J. 1986 Estimation of nonlinear transfer functions for fully developed turbulence. *Physica* D **20**, 320.

SCHUMM, M., BERGER, E. & MONKEWITZ, P. A. 1994 Self-excited oscillations and their control. *J. Fluid Mech.* **271**, 17.

THEILER, J., EUBANK, S., LONGTIN, A., GALDRIKIAN, B. & FARMER, J. D. 1992 Testing for nonlinearity in time series: the method of surrogate data. *Physica* D **58**, 77.

VAN ATTA, C. W. & GHARIB, M. 1987 Ordered and chaotic vortex streets behind circular cylinders at low Reynolds numbers. *J. Fluid Mech.* **174**, 113.

WILLIAM-STUBER, K. & GHARIB, M. 1990 Transition from order to chaos in the wake of an airfoil. *J. Fluid Mech.* **213**, 29.

WINANT, C. D. & BROWAND, F. K. 1974 Vortex pairing, the mechanism of turbulent mixing layer growth. *J. Fluid Mech.* **63**, 237.

WOLF, A., SWIFT, J. B., SWINNEY, H. L. & VASTANO, J. A. 1985 Determining Lyapunov exponents from a time series. *Physica* D **16**, 285.

ZAMAN, K. B. M. Q. & HUSSAIN, F. 1980 Vortex pairing in a circular jet under controlled excitation. Part 1. General jet response. *J. Fluid Mech.* **101**, 449.